Technical University of Munich
Physics Department

Bachelor's Thesis

Examination of Source Models for Particle Emission through Femtoscopic Analysis of K^+-p Correlations with ALICE at the LHC

by
Luca Italiano

Supervisors: Maximilian Korwieser, Marcel Lesch
First examiner (topic provided by): Prof. Laura Fabbietti
Second examiner: Prof. Susanne Mertens

15th of September 2023

Contents

Abstract

The unprecedented amount of high-energy proton-proton collisions at the LHC opened a new era to study the interaction between hadrons, involving strange or charm quarks. This was previously either difficult or impossible to access by traditional fixed target scattering experiments. One way to probe these interactions is femtoscopy, which requires a precise understanding of the particle-emitting source. Recent results from the ALICE Collaboration have shown that the size of this source exhibits a common scaling with the transverse mass $m_{\mathrm{T}} = \sqrt{k_{\mathrm{T}}^2 + \bar{m}^2}$ [1] for various baryon-baryon pairs (p−p and p−Λ). This in turn allowed to constrain the source for rarely produced pairs and, hence, to study the interactions of e.g. p−D [1], Λ−Ξ [2] and p−Ω [3].

In this thesis, the kaon-proton (K$^+$−p) correlation functions are extracted from data, with the goal to investigate whether the common source prescription is also appropriate to use in the case of meson−baryon correlations. The advantage of investigating K$^+$−p correlations for this study is twofold. Firstly, both particles are abundantly produced at the LHC and secondly the interaction is very well understood within chiral effective field theory. The experimental data about the K$^+$−p correlations are obtained by analysing pp collisions at a centre-of-mass energy of $\sqrt{s}$ = 13 TeV, collected by the ALICE collaboration at the LHC. A first estimate of the systematic uncertainties of the experimental correlation functions is provided.

To examine the properties of the particle emitting source in the K$^+$−p system, two models for the emission source are tested. Firstly, the resonance source model (RSM), which is a MC procedure to access the convolution of the Gaussian core source with the exponential decay functions of resonances, is tested. For two-particle correlations between baryons (p−p and p−Λ) [4] the RSM was already validated with great success and lead to the final-state-interaction studies of rarely produced pairs previously mentioned. The goal of this work is to ascertain whether the RSM can also be applied to constrain the source in the baryon-meson sector for K$^+$−p. Secondly, a new source model called CECA [5] is employed. CECA has only recently been developed, tested and finally validated for p−p and p−Λ correlations. In the context of this work, CECA is adapted to the K$^+$−p correlation and tested with data.

The compatibility of the model calculations with the data is estimated using the reduced χ^2 and yields the following results for CECA $\chi^2_{\mathrm{CECA}}/\mathrm{NDF} = 608/195 = 3.2$ and for RSM $\chi^2_{\mathrm{RSM}}/\mathrm{NDF} = 405/228 = 1.8$. The common scaling obtained within the RSM is compatible with the previous findings using baryon−baryon correlations, though exhibits a slight systematic underestimation of the fitted source sizes. The parameters obtained for the CECA model are possibly in tension with the results of the validation on the p−p and p−Λ correlations. However, these parameters currently miss systematic uncertainties and the optimization process needs to be refined before conclusive statements can be made.

[1] k_{T} denotes the average transverse momentum and $\bar{m}$ the average mass of the pair.

Chapter 1

Introduction

At the Large Hadron Collider, the collision of two particles can produce a multitude of new particles. The particles produced propagate away from the collision, interact with each other, and can be tracked by the LHC's detector experiments. Among these particles, a great deal of interest lies on the detection and study of rare particles involving strange and charm hadrons. Such studies are relevant e.g. to constrain the nuclear Equation of State (EoS) of neutron stars [6]. These are remnants of supernovae explosions, representing some of the most extreme stellar objects. They usually have radii of about 10-15 km and have masses of up to two solar masses [6]. On the other hand, the interaction of charm hadrons has found great interest. These studies are relevant to understand the rescattering of charm hadrons in the early phases of high-energy heavy-ion collisions as well as the study of exotic bound states like the T_{cc} [7]. Finally, also dynamically generated resonances like the $\Lambda(1405)$ and coupled-channel effects can be studied, for example in the $\mathrm{K^-{-}p}$ [8] and $\mathrm{p{-}\Lambda}$ [9] system. Due to their unstable nature, the interaction of strange and charm hadrons is difficult to study with classical scattering experiments. As such, the interaction of these particles with others is typically poorly constrained from the experimental side or unknown. One approach for investigating the interaction is femtoscopy, which is the analysis of correlations in the relative momentum space of particles [10]. These correlations are sensitive to the interaction within a particle pair, and also to the spacial relative distribution of the particles as they are created from the initial particle collision. This is described by the so-called source function $S(r^*)$ of the pair, where r^* is the relative distance between the two particles in their respective rest frame. Using the femtoscopic method, particle interactions can only be constrained tightly if the source function of the pair is well under control. This necessitates the development of models for the source in the hopes of understanding the particle production. This is deeply related to the understanding of the hadronisation process, which is the non-perturbative mechanism by which hadrons are formed.

The parametrisation of the source function depends on the model used to describe the evolution of the system starting from the collision to the evolution till hadronisation occurs. For example, the collision of heavy ions produces a plasma of free quarks and gluons, the constituents of hadronic particles, before forming into hadrons that propagate out from the collision site [11]. The behaviour of the quark gluon plasma (QGP) is well constrained by hydrodynamic models, in which the plasma expands with a common velocity before freezing out into a set surface from which it undergoes the hadronisation [12]. In heavy ion experiments, it is observed that the size of the source decreases as the transverse mass $m_\mathrm{T} = \sqrt{\bar{m}^2 + k_\mathrm{T}^2}$ increases, where $\bar{m}$ is the average mass of the particle pair and $k_\mathrm{T} = |\vec{p}_{\mathrm{T},1} + \vec{p}_{\mathrm{T},2}|/2$ is its transverse momentum. Furthermore, the scaling with the transverse mass appears to be common for different types of particle pairs [13]. In the heavy ion context, this can be explained as an effect of collective hydrodynamics, indicating a common expansion of the source as it evolves from the QGP phase.

Evidence of a common m_T scaling has also been observed for the particle pairs produced in proton-proton collisions, in particular for baryon-baryon pairs such as p-p and p-Λ [4]. The interpretation of this finding is still debated in the community of particle physicists, new data is needed in order to resolve the interpretation. The goal of this thesis is to examine the source function for the $\mathrm{K^+p}$ particle pair to see if the common scaling holds also for meson-baryon systems. Two different models for the source function will be tested, the Resonance Source Model (RSM) and Common Emission in CATS (CECA), to determine their applicability for describing the $\mathrm{K^+p}$ source.

Chapter 2

The femtoscopy method

Femtoscopy is the study of correlations between particles in the femtometre (10^{-15}) length scale. Its origins can be traced back to astronomy, where Brown and Twiss studied the correlations of signal intensities from stars to measure their size instead of looking at the signal amplitude itself [14]. This technique can be adapted to study particle interactions in collision experiments. Measurement of the kinematics of particle pairs produced in the collision can reveal information about the production mechanism and interaction of particles in the system [10].

A possible environment to conduct such femtoscopic measurements is the Large Hadron Collider (Ch. 3). There, protons are collided with centre of mass energies of a few TeV. Such a collision is known as an event. The high energy of the initial particles allows for the production of a large number of particles in an event. The initial product of the collision is a large number of partons, the constituents of hadrons. They propagate from the collision point and eventually form into hadrons in a process known as hadronisation. A hadron may undergo interaction with other nearby particles, altering the momentum of the particle pair. Some of the particles initially formed may have a short lifetime and decay into something more stable before they feel the effect of interactions with other particles. They are known as resonances and alter the spacial distribution of the interacting particles.

In this chapter, the application of the femtoscopic technique to access interactions will be discussed, both experimentally and theoretically. While the technique is applicable to many different particle pairs, this work concentrates on the femtoscopic analysis of proton and kaon pairs, produced in proton-proton collisions with a centre of mass energy $\sqrt{s}$ of 13 TeV. This is reflected in the choice of source parametrisation, interaction, and certain experimental effects.

2.1 Experimental determination of the correlation function

The central observable in the femtoscopic method is the correlation function $C(k^*)$ of the particle pair of interest. Two particles produced in the same event that are close in position and momentum space can interact with each other, and the correlation function is sensitive to this interaction. It is expressed as a function of the relative momentum k^* between the two particles in the pair rest frame, defined as

$$k^* = \frac{|\vec{p}_1^{\,*} - \vec{p}_2^{\,*}|}{2} \,. \tag{2.1}$$

Here, $\vec{p}_1^{\,*}$ and $\vec{p}_2^{\,*}$ are the momenta of the first and second particle of the pair, respectively. They are calculated in the pair rest frame, hence $\vec{p}_1^{\,*} = -\vec{p}_2^{\,*}$.

The correlation function can be accessed experimentally from the distributions of relative momenta of the particle pairs by employing a same and mixed event technique. It is defined as

$$C(k^*) = \mathcal{N} \cdot \frac{N_{SE}(k^*)}{N_{ME}(k^*)} \,. \tag{2.2}$$

In the latter equation, $\mathcal{N}$ is a normalisation constant and $N_{SE}(k^*)$ and $N_{ME}(k^*)$ are the same and mixed event momentum distributions, respectively [12]. Example plots for these are shown in Fig. 2.1. The same

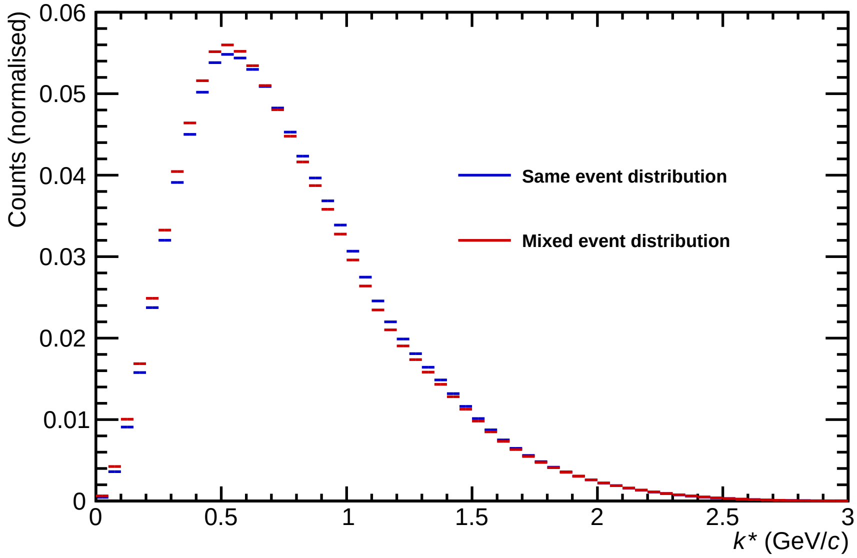

Figure 2.1: Example plots for same and mixed event momentum distributions. Both are normalised such that the area under the curve adds up to 1.

event distribution is obtained by sampling two particles from a single event and calculating their relative momentum k^*. The momentum distribution of the particle pairs is affected by their interaction, on top of any underlying phase space distribution present. The latter is the possible position and momentum states the particles assume independent of the interaction. To isolate the interaction from the underlying phase space, a mixed event distribution is used. This is obtained by sampling particles from different events with similar central properties such that they have the same phase space available. These properties include the event multiplicity, which is the number of particles produced in a single event, and the position of the collision in the detector. By sampling the two particles from different events, no interaction can occur between them and hence the distribution only stems from the available phase space. Therefore, dividing the same event distribution by the mixed event distribution retains only the effect the interaction has on the particle pair's k^*.

As the same and mixed event distributions may not have the same amount of statistic, the correlation function needs to be normalised in order for the effects of the interaction to be observable. The normalisation is performed such that the correlation function approaches unity in the momentum region where no interaction is present. In this case and region, both $N_{SE}(k^*)$ and $N_{ME}(k^*)$ should be equivalent. The range of the short-range strong interaction is of the order of 1 fm, which corresponds to a momentum of approximately 200 MeV$/c$ where the effect of the interaction is apparent in the correlation function.

The signature of the interaction is given by the shape of the correlation function, in particular how the correlation deviates from unity which corresponds to no interaction as described above (see Fig. 2.2). If the interaction is attractive, the pair tends to have a smaller relative momentum in their rest frame due to their attraction. As such, the correlation function is greater than unity for low k^* values. Analogously, a repulsive interaction results in a correlation function below unity for low relative momenta.

2.2 Theoretical determination of the correlation function

The correlation function is calculated theoretically using the Koonin-Pratt formula [12], given by

$$C(k^*) = \int S(\vec{r}^*)|\psi(\vec{r}^*, k^*)|^2 \, \mathrm{d}^3\vec{r}^* \, . \tag{2.3}$$

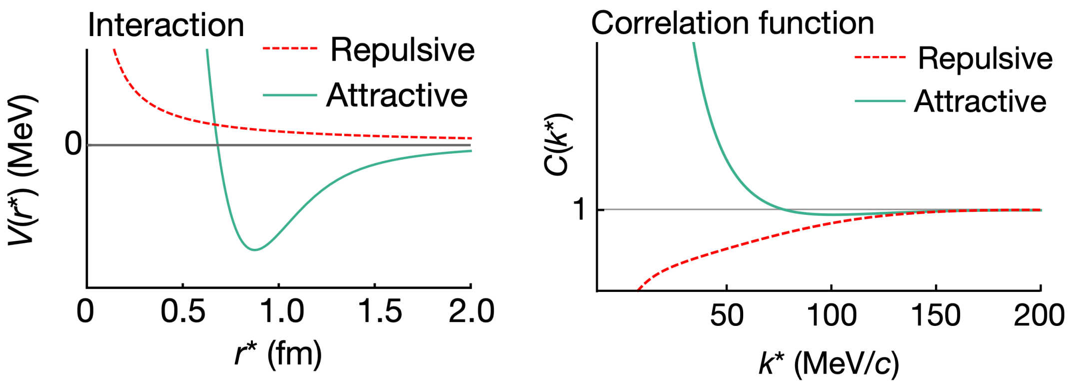

Figure 2.2: A example sketch for the possible shapes of a correlation function (right), for an attractive (green) and repulsive (red) interaction potential on the right [3]. The attractive interaction results in a correlation function above unity for low k^* values, while a repulsive interaction results in a function below unity. Both approach unity for high k^*.

The first term of Eq. (2.3) is the particle emitting source function, $S(\vec{r}^*)$, which is a function of the relative distance r^*. It describes the particle distribution at the time of emission from the hypersurface of hadronisation, just before the final state interaction (FSI) takes place. The second term is the two-particle relative wave function, $\psi(\vec{r}^*, k^*)$, of the particle pair, which includes the interaction between the particles [12]. The wave function is also subject to quantum statistics and should be symmetrised accordingly in the case of identical bosons or fermions, which is referred to as Hanbury-Brown and Twiss (HBT) effects.

The Koonin-Pratt equation is the connecting piece between theoretical models and experimental data. Given the wave function, into which the particle interaction is embedded, and the source function, the correlation function is obtained by solving Eq. (2.3). While this can only rarely be solved analytically, numerical integration done by CATS, discussed in Sec. 2.2.1, is utilised to determine $C(k^*)$. The theoretical correlation function can then be fitted to the experimental correlation function from Eq. (2.2) to determine free parameters in the source or interaction models.

As there are two components in the Koonin-Pratt equation that require a model as an input, assumptions about one need to be made to be able to determine the parameters of the other. If the focus of a femtoscopic analysis lies on constraining the interaction between particles in a pair, a source model will be chosen that includes the relevant experimental effects for the production of the particles of interest. For example, while a Gaussian model constrains the source for particles from heavy ion collisions [12], it is not an adequate model for the production of pions in proton-proton collisions as it does not account for any contributions from resonances [15]. Conversely, by looking at a particle pair with an interaction constrained well by theory, source models can be tested on data to better understand the physics behind the emission of said particles in a collision. In the case of the kaon-proton pair analysed in this thesis, the interaction is well constrained by chiral effective field theory (Sec. 2.2.3) [16], which allows for investigation of different model assumptions about the femtoscopic source.

2.2.1 Correlation Analysis Tool using the Schrödinger equation

The interaction between a particle pair is described by the Schrödinger equation, which needs to be solved to obtain the two-particle wave function. The Correlation Analysis Tool using the Schrödinger equation (CATS) is a framework which solves this equation using numerical methods and thus calculates the wave function for any given interaction potential [17]. If, for instance, the source model is to be tested in a system with known interaction, CATS is able to produce the wave function, solve (2.3) and provide the correlation function. In particular, the framework is able to provide precise predictions for the correlation function taking into account the non-asymptotic part of the interaction, as the full two-particle relative wave function is used as an input. This makes it an invaluable tool for the analysis of the kaon-proton particle pair.

2.2.2 Source models

The source function is the probability distribution of the relative distance between two particles at the moment the FSI begins. In the analysis of heavy ion collisions, the source function is typically assumed to have the form of a Gaussian

$$S(r^*) = (4\pi r_0)^{-3/2} \exp\left(-\frac{r^{*2}}{4r_0^2}\right) , \tag{2.4}$$

where r_0 is known as the source radius [12]. As has been observed in Pb-Pb collisions, the size of this radius is correlated to the transverse mass m_{T} of the particle pair, which is defined as

$$m_{\mathrm{T}} = \sqrt{k_{\mathrm{T}}^2 + \bar{m}^2} \, . \tag{2.5}$$

Here, $\bar{m}$ is the average mass of the two particles and

$$k_{\mathrm{T}} = |\vec{p}_{\mathrm{T},1} + \vec{p}_{\mathrm{T},2}|/2 \tag{2.6}$$

is the pair's total momentum transverse to the axis of the initial collision. The source size, extracted from data of proton pairs produced in Pb-Pb collisions, decreases as the transverse mass of the pair increases [18].

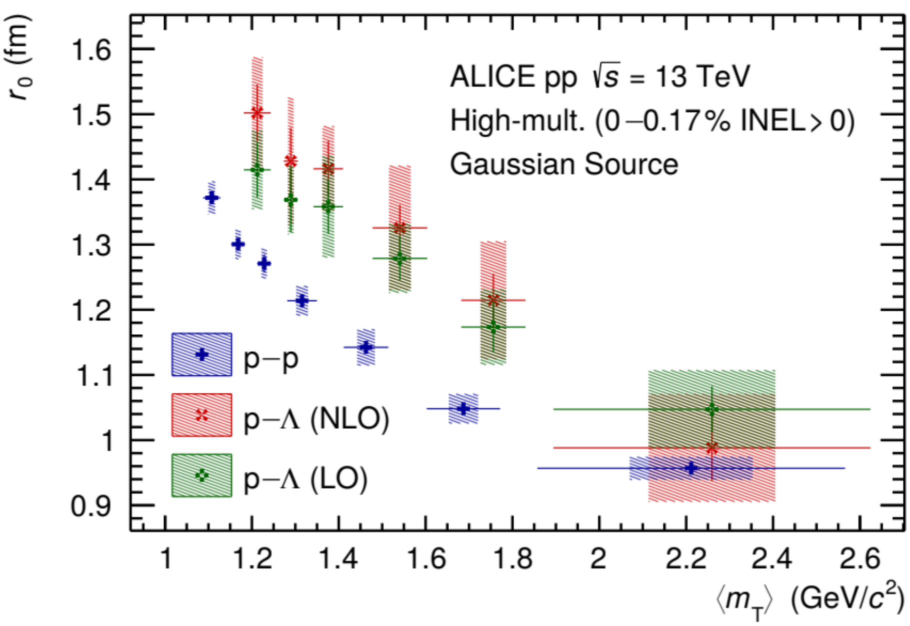

Figure 2.3: Source size r_0 for different m_{T} bins using the Gaussian source model [4].

This decrease in source size with increasing m_{T} is also observed for the p−p and p−Λ particle pairs resulting from proton-proton collisions (Fig. 2.3). Values for the source size are extracted by fitting the correlation function, obtained by CATS for a Gaussian source function, to experimental data. However, the Gaussian model operates under the assumption that all particles are produced in their final state, and feed-down via the decay of resonances into the particles of interest are neglected. Since the protons and Λ particles directly produced from hadronisation only account for 35.8% and 35.6% of their respective particle yields [4], the effect of resonances in this system is too large to be neglected by the source model. The reason for this is that the lifetime of the short-lived resonances is in the same order as the source size for pp collisions.

When employing a source model in which resonances are accounted for, the core source size, which is the length parameter in the Gaussian source function for the primordial particles, is investigated. The extracted core source sizes for different m_{T} bins for the p-p and p-Λ pairs exhibit the same scaling (Fig. 2.4). The question is whether a common source scaling holds for all particle types produced in proton-proton collisions. This is explicitly tested in this thesis for the baryon-meson sector with the K^+p system. In the following sections, the two source models used in this analysis, the Resonance Source Model (RSM) and Common Emission in CATS (CECA) model, will be introduced.

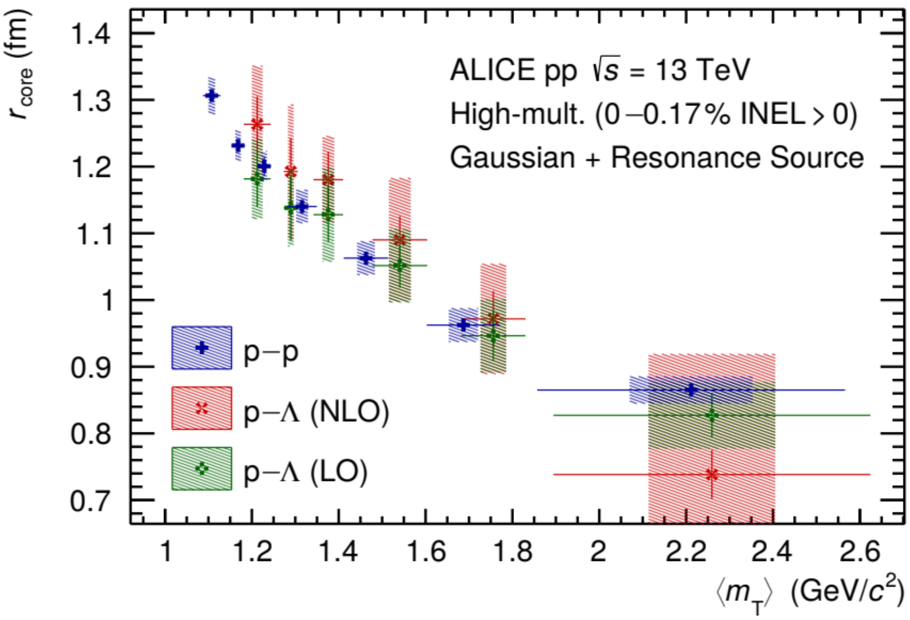

Figure 2.4: Source size r_0 for different m_{T} bins using the resonance source model [4].

Statistical Hadronisation Model

The distribution of resonances, used by both the RSM and CECA source models, is given by the Statistical Hadronisation Model (SHM). In this model, after the initial high-energy collision, the matter first forms into massive colourless objects known as clusters, which then break down into many individual hadrons [19]. The central postulate of SHM is that every possible many-hadron state possible within each cluster allowed by the conservation laws is equally likely, so the generation of the hadrons is a statistical process. Hence, the final state of a collision can be considered a non-interacting dilute gas of hadrons, which in particular will contain resonances that decay into the particles of interest. This so-called ideal hadron resonance gas (HRG) can then be treated with statistical methods.

The Thermal, Fast and Interactive Statistical Toolkit, or Thermal-FIST, is a *C++* package that estimates particle production for ideal HRG models [20]. It assumes a canonical ensemble for the ideal HRG and estimates the particle abundances expected for a pp collision at $\sqrt{s} = 13$ TeV, the parameters used for the calculation are summarized in Tab. 2.1.

From this, the abundances of the proton and kaon resonances are determined, given as a fraction of the total particle yield. The resonances with fractions of over 0.5% are given for protons and kaons in Tab. 2.2 and Tab. 2.3 respectively.

Ideal HRG model specifications	used
Ensemble	Canonical
Statistics	Quantum statistics for all particles
Resonance width	E dependent Breit-Wigner distr.
Breit-Wigner shape	Relativistic
Conservation laws	Canonical treatment of Baryon number (B), Charge (Q) and Strangeness (S)
Parameter	**Value**
Temperature (MeV)	171.0
Strangeness suppression factor	$\gamma_S = 0.78$
Flavour suppression factor	$\gamma_q = 1.0$
Source radius for one unit of rapidity (fm)	$R = 1.58$
Canonical correlated radius (fm)	$R_{\mathrm{c}} = 2.28$
B, Q, S	0

Table 2.1: Model specifications and values of parameters used for the yield calculations.

Particle	Mass (GeV/c^2)	$c\tau$ (fm)	Fraction (%)
K+	0.494	-	48.00
K*(892)0	0.896	4.16	15.75
K*(892)+	0.895	4.26	7.90
ϕ(1020)	1.019	46.36	6.05
K(1)(1270)+	1.253	2.19	2.35
K(1)(1270)0	1.253	2.19	1.93
K(2)*(1430)0	1.432	1.81	1.70
K(2)*(1430)+	1.427	1.97	1.29
K(1)(1400)+	1.403	1.13	1.19
K*(1410)+	1.414	0.85	1.10
K*(1410)0	1.414	0.85	0.98
K(1)(1400)0	1.403	1.13	0.96
f(2)'(1525)	1.517	2.29	0.70
f(1)(1420)	1.426	3.61	0.66
K(0)*(1430)0	1.430	0.73	0.65
R_{eff}(K+)	1.700	1.19	8.12

Table 2.2: List of resonances contributing at least 0.5% to the yield of K+. The first entry belongs to the primordially produced particle. These fractions are computed with Thermal-*FIST* for pp high multiplicity collisions at $\sqrt{s} = 13$ TeV. The resonances contributing less than 0.5% to the yield are averaged in R_{eff}(K+).

Particle	Mass (GeV/c^2)	$c\tau$ (fm)	Fraction (%)
p	0.938	-	36.00
Δ(1232)++	1.232	1.68	11.67
Δ(1232)+	1.232	1.68	7.97
Δ(1232)0	1.232	1.68	3.96
Δ(1600)++	1.570	0.79	2.28
N(1520)0	1.515	1.79	2.02
N(1520)+	1.515	1.79	1.74
Δ(1600)+	1.570	0.79	1.64
N(1675)+	1.675	1.36	1.33
Δ(1700)++	1.710	0.66	1.32
N(1440)0	1.440	0.56	1.24
N(1680)+	1.685	1.64	1.11
N(1680)0	1.685	1.64	1.11
N(1700)+	1.720	0.98	1.01
Δ(1620)++	1.610	1.52	0.96
N(1675)0	1.675	1.36	0.96
Δ(1600)0	1.570	0.79	0.95
N(1535)+	1.530	1.31	0.94
Δ(1700)+	1.710	0.66	0.94
N(1720)+	1.720	0.79	0.92
N(1440)+	1.440	0.56	0.91
Δ(1905)++	1.880	0.60	0.77
Δ(1950)++	1.930	0.70	0.74
N(1535)0	1.530	1.31	0.73
Λ(1520)	1.519	12.31	0.72
Δ(1620)+	1.610	1.52	0.69
Δ(1920)++	1.920	0.66	0.56
Δ(1905)+	1.880	0.60	0.55
Δ(1700)0	1.710	0.66	0.53
N(1875)+	1.875	0.98	0.53
Δ(1950)+	1.930	0.70	0.53
N(1650)0	1.650	1.58	0.52
Δ(1930)++	1.950	0.66	0.51
N(1650)+	1.650	1.58	0.50
R_{eff}(p)	1.889	0.84	11.68

Table 2.3: List of resonances contributing at least 0.5% to the yield of p. The first entry belongs to the primordially produced particle. These fractions are computed with Thermal-*FIST* for pp high multiplicity collisions at $\sqrt{s} = 13$ TeV. The resonances contributing less than 0.5% to the yield are averaged in R_{eff}(p).

Resonance Source Model

The key feature of the RSM is the inclusion of short-lived resonances which increases the effective source size, as previously described. After hadronisation, the initially produced particles, known as primordials, are either already a proton or kaon, or they are a resonance that will decay into a proton or kaon. The particles stemming from decays are known as the daughters of the primordials. Resonances with a sufficiently short lifetime ($c\tau_{\mathrm{res}} \lesssim 5$ fm) decay quickly and their daughter particle will still be spatially close to the other primordials and daughters produced during hadronisation [8]. This allows for FSI between these particles, which will alter the same event momentum distribution and contribute to the overall correlation. This leads to an increase in the effective source size as the exponential decays of resonances result in exponential tails in the source function.

The source function contains contributions from the many different resonances given by Thermal-FIST. After building the source, the individual contributions are not discernible in the overall function describing the source, but rather the effect of the resonances as a whole increases the source size. The assumption that the overall source function is properly averaged over all individual resonance contributions

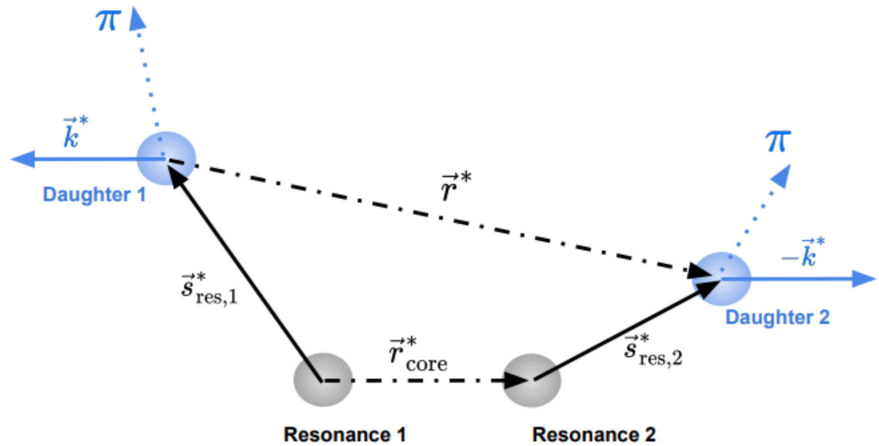

Figure 2.5: Illustration of the enlargement of the effective source sizes in RSM through the decay of resonances into their daughter particles [4].

motivates the use of effective resonances. For protons and kaons each, the masses and lifetimes of all decay channels feeding into the source, weighted with their abundances relative to each other, are averaged to create two effective resonances. For protons (kaons), this effective resonance has a mass of $M_{\text{res}} = 1.362$ GeV/c^2 ($M_{\text{res}} = 1.050$ GeV/c^2) and a lifetime of $\tau_{\text{res}} = 1.65$ fm/c ($\tau_{\text{res}} = 3.66$ fm/c) [8]. This massively reduces the number of possible resonance-primordial and resonance-resonance pairings, which would otherwise need to be calculated if individual resonances are used instead of averaged ones.

The source function is built by generating primordials, propagating any resonances, and then determining the relative distance within each particle pair. In the RSM, the spatial distribution of the primordial particles is assumed to that of the Gaussian from Eq. (2.4) with the initial distance parameter $\vec{r}^*_{\text{core}}$. Then, the resonances propagate for a time t_{res} obtained by sampling from an exponential distribution based on their lifetime τ_{res} before decaying into a proton or kaon, with a pion assumed as the byproduct of the decay [4].

The maximal modification to the source function would occur in the case of back-to-back emission, where the resonances in a particle pair propagate in opposite directions in the lab frame. This would ensure the largest possible distance between proton and kaon when the resonances decay into their end products. However, as not all emissions are back-to-back, the transport model framework EPOS [21] is used for a more realistic modelling of the propagation kinematics. EPOS simulates particle production in proton-proton collisions at $\sqrt{s} = 13$ TeV which lie within the track selections used for the experimental data (see Sec. 4.2). The particles included in the simulation have been selected to reproduce the mass and lifetime of the effective resonances used by the resonance source model. Based on EPOS, the magnitude and orientation of the resonance momentum, $\vec{p}^*_{\text{res}}$, with respect to its partner, is determined.

After the propagation of their mother resonance, the protons and kaons produced through decays will be displaced by the vector

$$\vec{s}^*_{\text{res}} = \vec{\beta}^*_{\text{res}} \gamma^*_{\text{res}} t_{\text{res}} = \frac{\vec{p}^*_{\text{res}}}{M_{\text{res}}} t_{\text{res}} \,. \tag{2.7}$$

For protons and kaons created primordially, it is assumed that $\vec{s}^*_{\text{res}} = \vec{0}$, so these are not propagated. This leads to an overall distance of

$$\vec{r}^* = \vec{r}^*_{\text{core}} - \vec{s}^*_{\text{res},1} + \vec{s}^*_{\text{res},2} \tag{2.8}$$

between the two particles at the moment the FSI begins. At this point, the system is boosted into the kaon-proton pair rest frame and the relative momentum of the particles is determined. To restrict the source function to only include pairs within the femtoscopic momentum region, pairs with a relative momentum above $k^* = 200$ MeV/c are rejected. If not rejected, the pair's relative distance $\vec{r}^*$ is used to build the source function.

The generation procedure is done for all four particle pair possibilities: primordial-primordial, decay-primordial, primordial-decay, and decay-decay. Their probabilities of occurring are P_1P_2, $\tilde{P}_1P_2$, $P_1\tilde{P}_2$ and $\tilde{P}_1\tilde{P}_2$ respectively, where $P_{1,2}$ are the primordial fractions and $\tilde{P}_{1,2} = 1 - P_{1,2}$ are the fractions of particles stemming from resonances [4]. By sampling the relative distance, the source function is created for each of the four particle pair arrangements, which are then weighted by their probabilities to build the total source

$$S(r^*) = P_1P_2 \times S_{P_1P_2}(r^*) + \tilde{P}_1P_2 \times S_{\tilde{P}_1P_2}(r^*) + P_1\tilde{P}_2 \times S_{P_1\tilde{P}_2}(r^*) + \tilde{P}_1\tilde{P}_2 \times S_{\tilde{P}_1\tilde{P}_2}(r^*)\,. \tag{2.9}$$

The RSM source is compared to a Gaussian source of the same core radius in Fig. 2.6. While both exhibit a similar Gaussian core for smaller r^* values, the effect of the resonances becomes apparent in the RSM source function for large r^*, where the function exhibits an exponential tail.

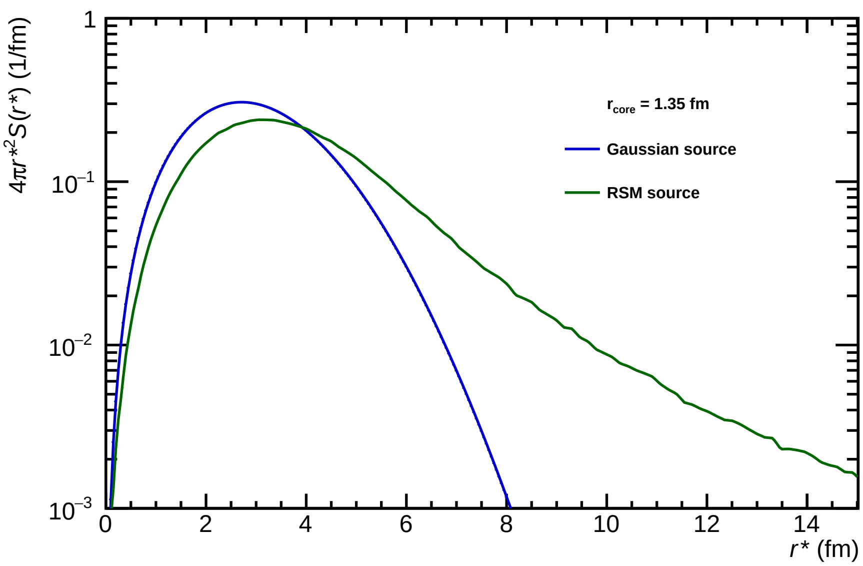

Figure 2.6: A comparison of the RSM source function with a purely Gaussian source with the same r_{core}. The exponential tail in the RSM source is due to the effective resonances.

Common Emission in CATS

The CECA [5] model is an effective model of the particle emission working on the level of single particles, accounting for possible collective effects. Like in the RSM, the effect of short-lived resonances is modeled by computing the decay of the resonance according to the branching ratio and an exponential distribution based on their lifetime. CECA offers several technical advantages compared to the RSM, most importantly no external input from an event generator is needed and effects due to the Lorentz boost of feed-down particles are taken into account. Additionally, as CECA is based on single particle emission, it can be generalised to future three-body femtoscopic studies.

The usage of CECA requires the definition of a data bank which contains the momentum distributions, relative abundances, decay channels, and branching rations of the particles of interest and all resonances which may decay into the studied pair. The abundances are estimated like in the case of the RSM by calculations within the HRG model [20], the branching ratios as well as the hadronic cocktail are informed by the measured resonance spectrum listed in the Particle Data Group summary. The momenta distributions are obtained by calculating the p_{T} spectrum from a blast-wave model and assuming a uniform distribution in the azimuthal angle $0 < \phi < 2\pi$ and pseudorapidity $|\eta| < 0.8$, where η is defined as $-\ln\tan(\theta/2)$ with the polar angle θ. The value of the model parameters for the blast-wave are taken from Ref. [22] and obtained by fitting hadron spectra measured in pp collisions at $\sqrt{s} = 13$ TeV by the ALICE collaboration. The sampling from the data bank to generate the source distribution can be understood as

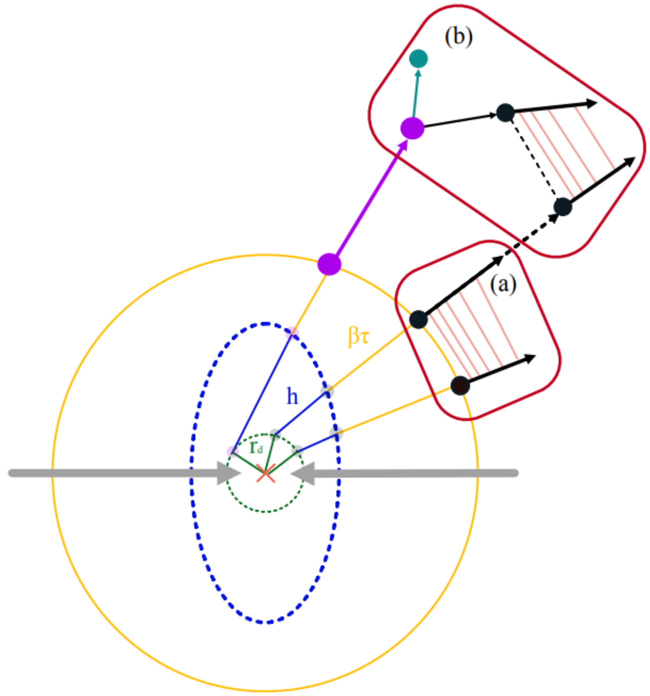

Figure 2.7: Schematic overview of particle emission in the CECA model [5].

randomly selecting a four-vector according to the abundance and kinematic distributions.

Figure 2.7 illustrates the emission as modeled with CECA for a pp collision in 2D. Besides the configuration of the data bank, the dynamics in the model are fully controlled by the three parameters ($\vec{r}_{\mathrm{d}}$, $\vec{h}$ and τ). The initial space coordinate is sampled from a Gaussian distribution of width $|\vec{r}_{\mathrm{d}}|$ centered around the collision center marked by the red cross. This conforms to the assumption that the initial parton scattering is randomly displaced by $\vec{r}_{\mathrm{d}}$ (green dashed line), referred to as *displacement point*. Within CECA the QCD constituents are not modeled explicitly, however, for all hadrons containing only u,d and s quarks a common hadronisation surface is assumed. This allows to model a collective expansion of the system. The hadronisation surface is defined by the profile of an ellipsoid, centered around the displacement point $\vec{r}_{\mathrm{d}}$, and effectively parameterized by the so-called *hadronisation parameter* $\vec{h}$ (dashed blue line). The point of hadronisation is determined by the sum of $\vec{r}_{\mathrm{d}}$ and $\vec{h}$. At this point the particles are assumed to acquire their on-shell mass and momentum, meaning a four-momentum is randomly sampled according to the specifications in the data bank. One assumption in femtoscopy is that the measured pairs are subject to the FSI and hence have a well defined wave function, which has no significant overlap with any other wave function. This is achieved by propagating each particle along a straight line according to the sampled velocity $\vec{\beta}$ for a fixed amount of time τ. This re-scattering phase is assumed to leave the momenta of the particles unchanged. After this step the particles are considered to be "emitted" and the final spacial coordinate is used to build up the primordial source, in case no resonance was sampled. This source distribution is evaluated in terms of the relative distance $r*$ in the pair rest frame (PRF) and corresponds to scenario a) in Fig. 2.7. However, only particle pairs with a relative momentum $k^* < 200$ MeV/c are taken into account.

An example of the modification of the primordial source due to the presence of a short-lived resonance (solid purple circle) is shown in scenario b) in Fig. 2.7. The resonance is propagated according to an exponential distribution based on the lifetime and decayed. The formalism of femtoscopy requires that the particles making up the studied pair are emitted at equal times. Therefore in-case a pair is built containing at least one feed-down particle, the other particle is propagated along a straight line until the time component of emission is equal to the time of the partner particle. This correction is applied on the level of pairs and ensures that the equal time condition of femtoscopy is fulfilled. After the times are equalized the source distribution of the primordial-resonance and resonance-resonance case is evaluated in the PRF.

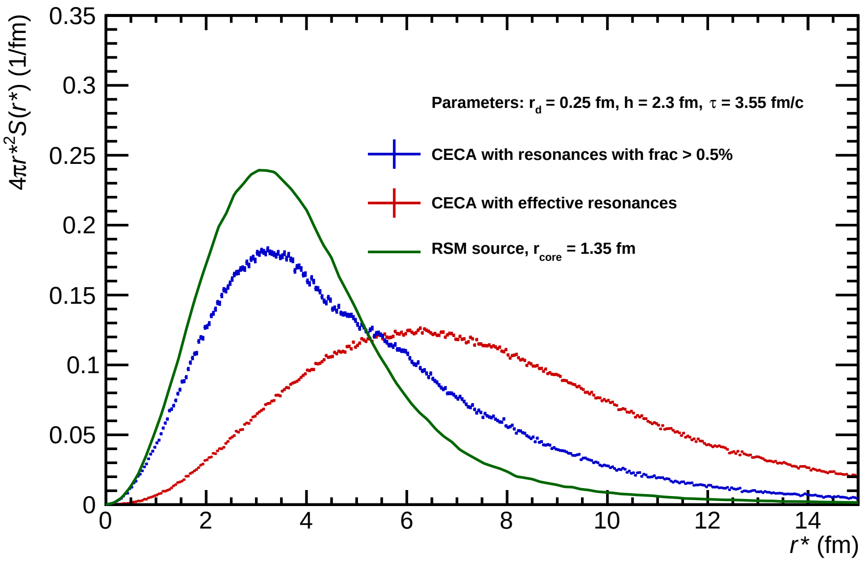

Figure 2.8: A comparison of source functions generated in the CECA model. Shown in blue is the source function when including all individual resonances with a fraction of over 0.5% in CECA. Shown in red is the source function generated when CECA uses only effective resonances. These are compared to an example RSM source function, shown in green.

The study presented in Ref. [5] showed that a single choice of $\vec{r}_{\mathrm{d}}$, $\vec{h}$ and τ is capable to fit the m_{T} differentially measured p−p and p−Λ correlation functions. Further more Ref. [5] relates the m_{T} scaling to the radial expansion of the collision system, this is in contrast to the RSM where each m_{T} range is fitted separately. One goal of this work is to determine whether the same or a different set of parameters is also able to fit the m_{T} differentially measured K−p correlations. This would show that CECA can also be used for meson−baryon correlation studies for which modifications of the source distribution due to resonances are pertinent.

Pictured in Fig. 2.8 are two source functions generated with CECA for an example set of parameters. If CECA is given only two effective resonances, corresponding to those used in the resonance source model, the resulting source function (red) extends over a large range and its mean is shifted to large r^* values. If CECA is instead supplied with all proton and kaon resonances which have a fraction above 0.5%, the source function (blue) is a more comparable to RSM sources with typical radii observed in proton-proton collisions.

2.2.3 Chiral effective field theory

The non-perturbative behavior of Quantum Chromodynamics (QCD) at low energies becomes manifest through the confinement of quarks (q) and gluons within observable, colour-neutral states, which we recognize as hadrons. Therefore computing the nuclear force between hadrons, composite particles held together by the strong force, from first-principles remains one of the most formidable challenges in contemporary theoretical particle physics. Instead, using an effective field theory approach, in which the hadrons, namely baryons (qqq) and mesons ($q\bar{q}$), are the degrees of freedom, was developed in the early 1990s by Weinberg [23].

The main idea behind the chiral effective field theory (χEFT) is to start from the most general Lagrangian density (for brevity there will be no distinction between the Lagrangian and the Lagrangian density) obeying the global symmetries of the QCD Lagrangian. In general the Lagrangian is invariant under transformation of global symmetries and these in-turn restrict the possible terms inside the Lagrangian [24]. In the limit of vanishing quark masses the chiral symmetry is realized and the Lagrangian attains a simpler form as the mass terms are zero, details are found in Ref. [24]. Incorporating baryons and mesons as the degrees of freedom and applying a momentum cut-off leads to the formulation of a Lagrangian that preserves chiral symmetry and is valid only up to a certain energy scale, hence the name effective field theory.

The strong interaction between the kaon and the proton is well understood within the framework of χEFT [25, 26]. It was already used to successfully describe correlations between kaons and protons [8], which makes the kaon proton system an ideal laboratory to constrain the particle emitting source for meson−baryon correlations.

Chapter 3

Experimental setup

3.1 The Large Hadron Collider

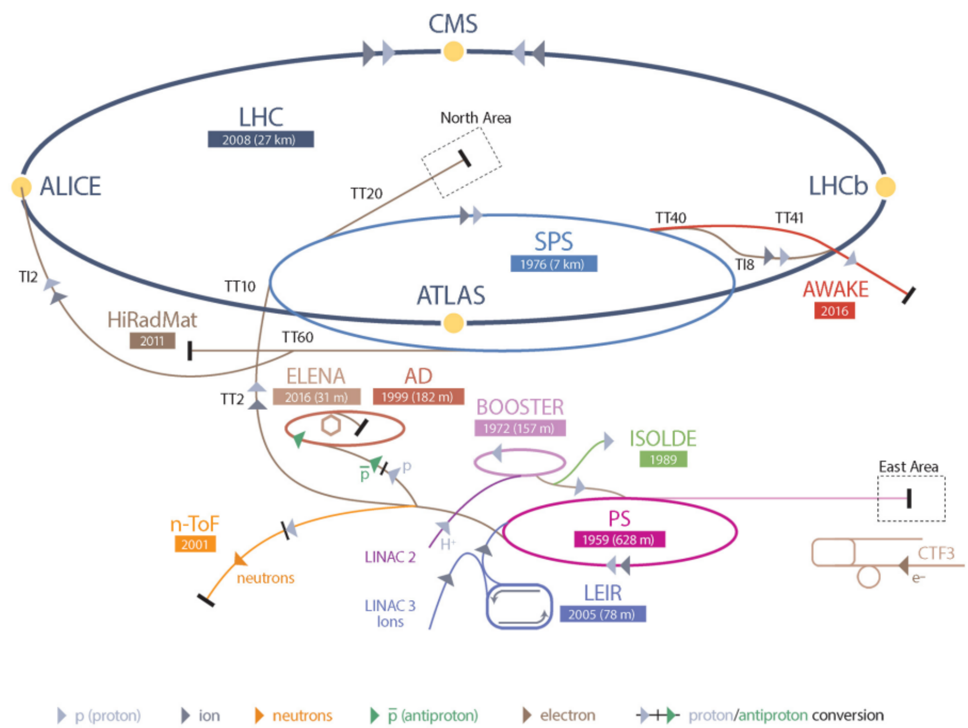

Figure 3.1: Overview of the accelerator system at CERN [27].

The Large Hadron Collider (LHC) is a particle accelerator used for high-energy nuclear collisions. It is located at the European Organisation for Nuclear Research (fr. former "Conseil Européen pour la Recherche Nucléaire" - CERN) and placed in the circular tunnel formerly used for the Large Electron-Positron Collider (LEP). The LHC has a circumference of 26.7 km [28]. The accelerator obtains protons at an energy of 450 GeV from a chain of pre-accelerators (Fig. 3.1) which includes the accelerators Linac 2, Proton Synchrotron Booster (PSB), Proton Synchrotron (PS), and the Super Proton Synchrotron (SPS). Upon reaching the LHC, they are split into two beams that collide with each other at one of the so-called interaction points. Superconducting dipole magnets cooled to temperatures of 1.9 K provide a magnetic field of up to 8.3 T to keep the proton beams on the circular track while the quadrupole magnets are used for beam focusing. Within the LHC, the proton beams are further accelerated up to energies of 7 TeV per beam. The collisions are possible at four different interaction points, each equipped with a different experiment: ATLAS, CMS, LHCb, and ALICE. The data for this analysis is taken from the LHC Run 2 data taking period, a proton-

proton collision campaign performed at ALICE from 2015 to 2018 with a centre of mass energy $\sqrt{s}$ of 13 TeV [27].

3.2 A Large Ion Collider Experiment

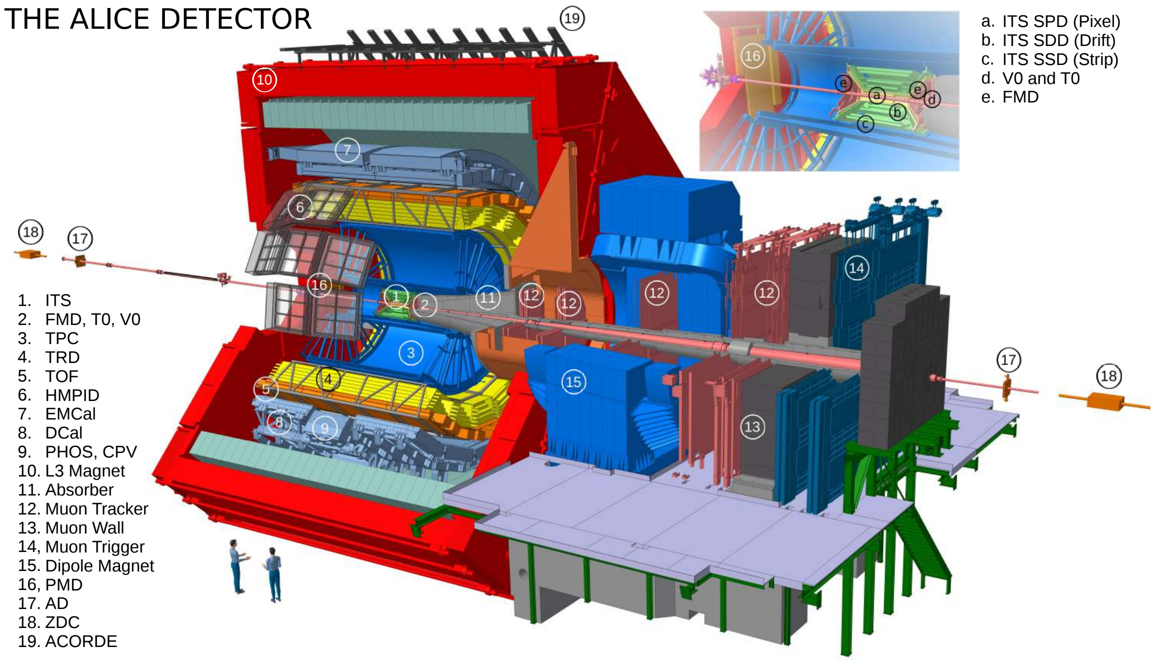

Figure 3.2: Overview of the ALICE detector system [29].

A Large Ion Collider Experiment, or ALICE, is the particle detector system located at the second interaction point of the LHC. It is the only dedicated heavy-ion experiment located at the LHC with the goal of analysing the creation of QCD (quantum chromodynamics) matter in collisions of lead nuclei at high energy. However, complementary to the heavy ion studies, proton-lead (pPb) and proton-proton (pp) collisions are studied by ALICE. This helps to identify QCD matter signals in order to understand the collision dynamics but also allows the study of the other physical phenomena such as residual strong interaction with femtoscopy [30].

ALICE is composed of a layered detector system (Fig. 3.2) used for particle identification and reconstruction of the collision vertex, i.e. the position of the initial pp collision, and particle tracks. The detectors relevant for this analysis are embedded in the L3 solenoidal magnet with a field strength of $B = 0.5$ T, located within the central cylindrical barrel of ALICE. This bends the trajectories of the charged particles due to the Lorentz force, increasing the length of the tracks and allowing for better reconstruction. The innermost central-barrel detector is the Inner Tracking System (ITS), followed by the Time Projection Chamber (TPC), Transition Radiation Detector (TRD) and Time-of-Flight (TOF) detector. The barrel is aligned with the beam direction and the detectors cover the full azimuthal angle around the beam as well as the midrapidity polar angle range of $|\eta| < 0.9$, where θ is the angle between particle momentum and the beam direction. Further out, these are complemented by the Photon Spectrometer (PHOS), Electromagnetic Calorimeter (EMCal), and High Momentum Particle Identification Detector (HMPID). Outside of the central barrel, the ACORDE detector, which detects cosmic rays, is located.

ALICE also has a number of forward detectors, which are located along the beam axis. These include the T0 detector, a Cerenkov detector system which measures the time of each event [30], that is then used to calculate the time of flight with the TOF detector. Another forward detector is the plastic scintillator detector V0, which measures the charged particle multiplicity of each collision and can act as a trigger for high-multiplicity events [31], as is used in the selection of events for this analysis (see Sec. 4.1).

The ITS, TPC and TOF detectors provide the particle identification (PID) and track reconstruction for this analysis. These will be explained in further detail in the next sections.

3.2.1 Inner Tracking System

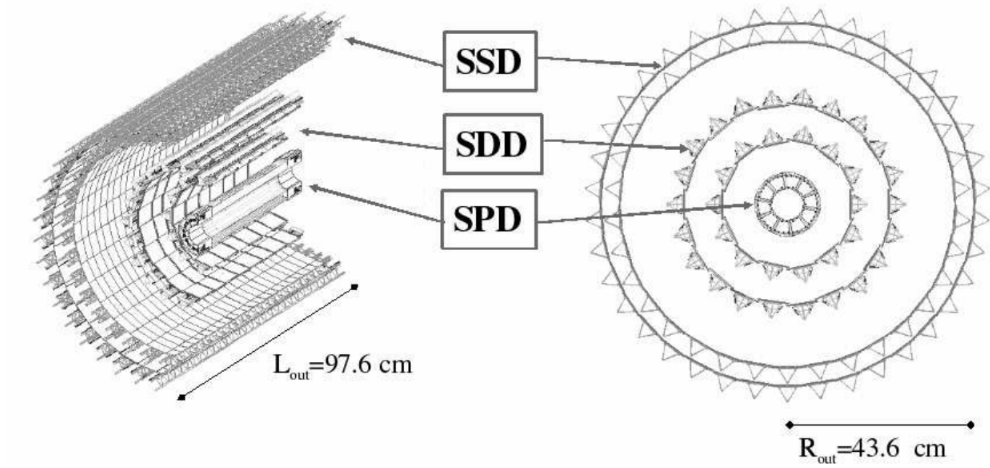

Figure 3.3: Overview of the layers of the ITS [32].

The ITS is the detector system closest to the beam and is comprised of six layers of semiconductor detectors with radii between 3.9 and 43 cm (Fig. 3.3). The ITS is used to determine the primary vertex of the collision within ALICE, which is achieved with a resolution better than 100 μm [33]. In addition to this, the ITS is used for the reconstruction of the position of particle decays, so-called secondary vertices. This reconstruction done by the ITS assists that done by the TPC and is especially useful for reconstructing tracks in the dead zone of the TPC, increasing the statistic yield of an event.

The two inner layers consist of the Silicon Pixel Detectors (SPD) and employ hybrid silicon pixel technology to identify the position of the primary and secondary vertices. A total of $9.8 \cdot 10^6$ pixel cells, each with an area of $50 \times 425\ \mu\mathbf{m^2}$, are used for these layers. This fine granulation is needed as the SPDs are very close to the collision point and the track density is therefore very high. The following four layers of the ITS are two layers of Silicon Drift Detectors (SDDs) and two layers of Silicon Strip Detectors (SSDs). These are used for tracking and PID within the ITS by measuring the particles' energy loss per distance travelled, in particular for tracks with a transverse momentum $p_{\mathrm{T}} \leq 0.7$ GeV/c [30, 34].

3.2.2 Time Projection Chamber

The TPC is a cylindrical gas detector spanning radii of 85 to 247 cm from the beam, and is used for particle tracking and identification [35]. Its structure can be seen in Fig. 3.4. The detector covers the full azimuthal angle and the pseudorapidity range of $|\eta| < 0.9$. It consists of a conducting electrode, located in the longitudinal centre of the barrel and charged to a potential of 100 kV. This creates an axial electric field of 400 V/cm within the TPC. A charged particle traversing the detector ionises the Ne-CO_2-N_2 gas along its trajectory and the resulting electrons are accelerated towards its endplates due to the electric field. The choice of gas is motivated by its good diffusion properties, low ionisation energy, and low chance of multiple Coulomb scattering to keep the initial propagating particle on its course. The resulting positive ions in the gas are also able to clear out quickly from the TPC volume [35].

The two endplates are divided into 18 trapezoidal sectors each which consist of Multi-Wire Proportional Chambers (MWPCs). As the drifting electrons approach the anode wires of the MWPC, they ionise the gas further and produce an avalanche of electrons which results in an electrical current registered by the pad of the MWPC. From the position and time information of the signal, the track can be reconstructed. In addition to this, the TPC also provides energy loss measurements to be used for particle identification for

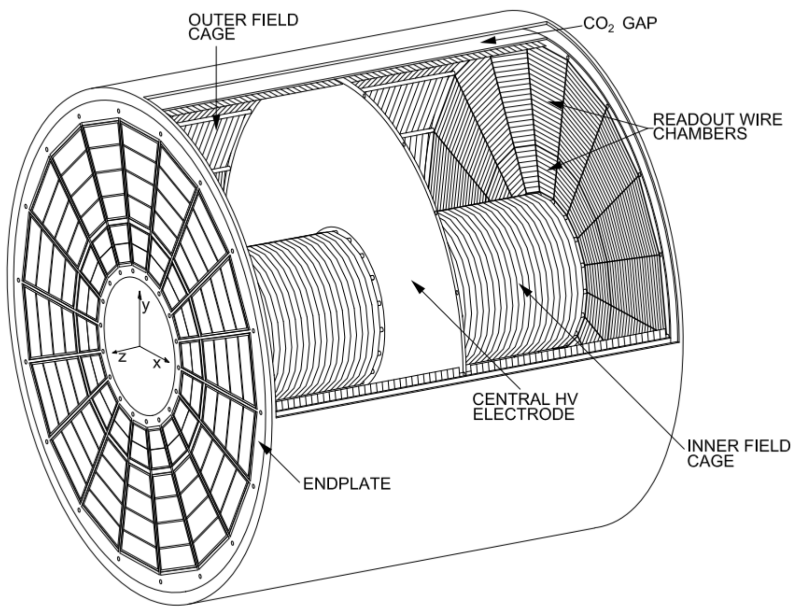

Figure 3.4: Sketch of the TPC detector in ALICE [35].

charged hadrons. Particles can be identified by using the Bethe-Bloch formula

$$-\frac{\mathrm{d}E}{\mathrm{d}x} = \frac{4\pi n z^2}{m_e c^2 \beta}\left(\frac{e^2}{4\pi\varepsilon_0}\right)^2 \left[\ln\left(\frac{2m_e c^2\beta^2}{I\cdot(1-\beta^2)}\right) - \beta^2\right]. \tag{3.1}$$

In the latter equation, ze is the charge, v the speed, and $\beta = v/c$ the beta factor of the particle traversing the detector medium, while n is the electron number density, m_e the mass of an electron, and I the mean excitation level of the medium being traversed. As a function of v, the $\mathrm{d}E/\mathrm{d}x$ curves are the same for all particles with the same charge since the other variables depend only on the medium. The momentum is calculated from the speed as $p = \gamma m v$ with the Lorentz factor $\gamma = 1/\sqrt{1-\beta^2}$, with the only other parameter being the particle mass m. This means that separate curves will form for particles with different masses when $\mathrm{d}E/\mathrm{d}x$ is plotted as a function of p rather than v (Fig. 3.5). Particle identification is done by assessing how close a track's energy loss is to the theoretical Bethe-Bloch curve of a given particle, which is given by the number of standard deviations

$$n_{\sigma,\mathrm{particle}} = \frac{(\mathrm{d}E/\mathrm{d}x)_{\mathrm{Bethe-Bloch}} - (\mathrm{d}E/\mathrm{d}x)_{\mathrm{TPC}}}{\sigma_{\mathrm{d}E/\mathrm{d}x}} \tag{3.2}$$

In the case of the TPC, the separation of the bands corresponding to different types of particles is largest below p_T 0.7 GeV/c, but the TPC also provides capabilities for particle identification up to 20 GeV/c [30]. During LHCs long shut down from 2019 to 2021, the MWPCs have been replaced by Gas Electron Multipliers (GEMs) within the TPC [36]. This allows the detector to cope with the higher interaction rates of the LHC Run 3.

3.2.3 Time Of Flight

The TOF detector is the outermost detector utilised in this analysis. It spans the radii from 3.7 to 3.99 metres, the pseudorapidity range of $|\eta| < 0.9$ and the full azimuthal range. The detector provides additional information for particle identification, in particular for protons up to $p_\mathrm{T} \approx 4$ GeV/c and kaons up to $p_\mathrm{T} \approx 2.5$ GeV/c [30].

The design is based on Multigap Resistive Plate Chambers (MRPCs), which consist of stacks of five gas gaps in between resistive glass plates. Charged particles passing through the MRPC ionise the gas, leading to an electron avalanche which is accelerated to the readout pads by the MRPC's electric field [38]. The large number of gaps in each MRPC is to ensure a high detector efficiency while the gaps between glass

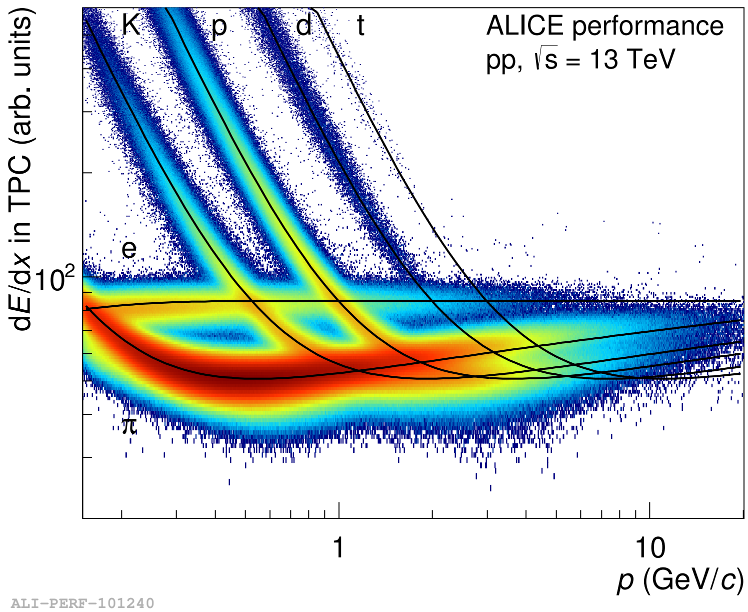

Figure 3.5: Measurement of the specific energy loss dE/dx with the TPC used for particle identification [37].

layers are kept small in order to achieve a very small time resolution of 56 ps. The chambers are arranged into 1593 strips, each with 48 pickup pads. Two MRPCs are always stacked on top of each other to further increase the number of layers, resulting in 96 readout pads per strip and 152928 in total [39].

To calculate the time of flight of the particles from an event, the time at which the event occurred must first be determined. This is done in the TOF setting by the T0 detector, an additional detector system consisting of a Cerenkov counter on each end of the ALICE interaction point [30]. After determining the event time, this is subtracted from the time at which the track reaches the TOF detector pads to calculate the time of flight. The length each particle travelled to get to the detector is divided by this time of flight to obtain the velocity of the particles. Since the momentum $p = \gamma m v$ depends only on particle mass and velocity, measuring the velocity in the TOF and comparing it with the momentum measured in the TPC is sufficient for determining the mass. Velocity and momentum are plotted for each registered hit in the detector and compared to theoretical curves obtained by plotting the momentum-velocity relation for known particles of different masses (Fig. 3.6). This allows for an n_σ determination akin to Eq. (3.2) with the Bethe-Bloch method of the TPC.

3.3 Track reconstruction

Reconstruction of tracks in ALICE is performed using the Kalman filter technique with the detector readouts [32]. For a registered hit in a TPC pad, the state vector of the measured track parameters and the covariance matrix, which includes the position and momentum resolution of the pad, is used to propagate to another row of pads. If a different hit is compatible with the current track information, it is added and the information is updated. This process is repeated to construct a complete TPC track, the so-called TPC-only track. The tracks can also be propagated to other tracking detector elements, such as the ITS and TRD, where this process is continued to reconstruct a global track and to determine the position of the primary vertex. The different types of tracks are accessed by the different filterbits used in the track selections in Sec. 4.2.

3.4 Monte Carlo simulations

Additionally, to experimentally collected data, general purpose Monte Carlo (MC) simulations of events, which were filtered through the ALICE detector, tuned to the conditions during the LHC Run2 campaign,

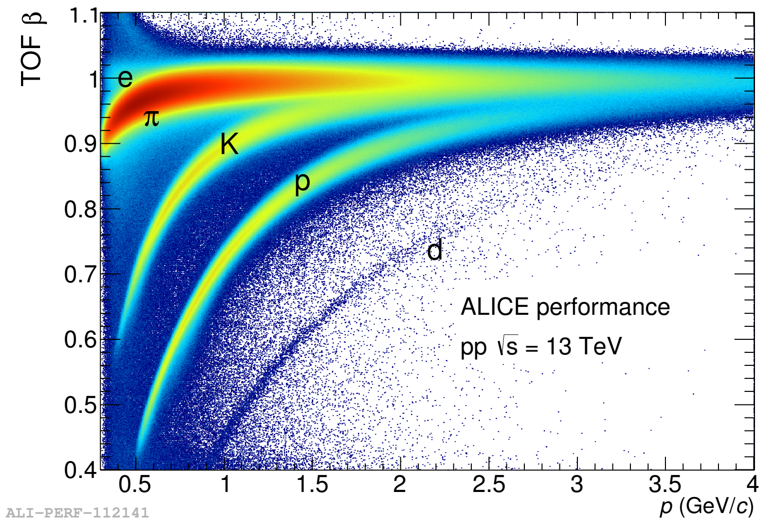

Figure 3.6: Measurement of β against particle momentum with the TOF detector [40].

and the reconstruction algorithm, are used. The MC simulation, is done in a two-step process using Phythia 8.2 and GEANT3 [41, 42]. Particle generation, the decay of resonances and propagation is done with Phythia. The generated particles are than handed to a GEANT3 simulation of the ALICE detector. The simulated data can then be processed analogously to the experimental data, with the same track and event selections. The MC simulations are suitable to study the momentum resolution of the detectors as well as the fractions and purities needed for the λ-parameters described in Sec. 4.4.

Chapter 4

Data analysis

4.1 Event selection

The data used for this analysis was recorded during the LHC Run 2 data taking period of 2015-2018. The analysed events consist of proton-proton collisions at $\sqrt{s} = 13$ TeV measured with ALICE. To increase the quality of the dataset and remove data which is not suitable for the analysis, a number of event selections are applied, which are summarised in Table 4.1. The kHighMultV0 trigger ensures that only events which register as high multiplicity in the V0 detector are accepted. High multiplicity events are used as they have a larger yield of strange particles, including the charged kaon investigated here [43]. The z coordinate of the primary event vertex, as determined from track reconstruction, should be within 10 cm of the nominal ALICE interaction point. The latter is defined as the point along the beam axis in the middle of the ALICE barrel detector in the longitudinal direction. This ensures a good detector acceptance as events far away from the nominal interaction point might not fully be reconstructed which could lead to biases, for example for the estimated event multiplicity.

The two vertex positions determined by the global tracks and SPD-only tracks, as described in Sec. 3.3 should agree within 0.5 cm, with the SPD-determined vertex having a resolution better than 0.25 cm. When determining the vertex from the reconstructed global tracks, at least two tracks are required, while one is sufficient for the determination of the primary vertex from SPD information. An additional concern is pile-up, where multiple p-p collisions occur close in time and position. This makes the track reconstruction unreliable as it becomes difficult to discern which event each track belongs to, and as a result such events are rejected.

The transverse sphericity S_{T} characterises the shape of the event [44]. The sphericity distribution of the data before selections is shown in Fig. 4.1. Events with S_{T} approaching 1 are isotropic and have tracks propagating in all directions. Events with S_{T} approaching 0, known as "pencil-like" events, are dominated by jets, which stem from one high energy particle breaking off into multiple particles with momenta in the same direction. An event having a low sphericity may indicate that two partons from the initial collision have

Selection criteria	Value
Trigger	kHighMultV0
z vertex	$\lvert \mathrm{vtx}_z \rvert < 10$ cm
Contributors to track vertex	$N_{\mathrm{contrib,track}} > 1$
Contributors to SPD vertex	$N_{\mathrm{contrib,SPD}} > 0$
Distance between track and SPD vertex	$d_{\mathrm{vtx,track-SPD}} < 0.5$ cm
SPD vertex z resolution	$\sigma_{\mathrm{SPD,z}} < 0.25$ cm
Pile-up rejection	AliVEvent::IsPileUpFromSPD() AliEventUtils::IsSPDClusterVsTrackletBG()
Sphericity	$0.7 < S_{\mathrm{T}} < 1.0$

Table 4.1: Summary of event selections applied to Run 2 dataset.

Selection criteria	Value
Filterbit	128 (TPC only tracks)
Transverse momentum	$0.5 < p_{\mathrm{T}} < 4.05$ GeV/c
DCA vertex position	$\mathrm{DCA}_{\mathrm{xy}} < 0.1$ cm $\mathrm{DCA}_{\mathrm{z}} < 0.2$ cm
Pseudorapidity	$\lvert\eta\rvert < 0.8$
Number of TPC clusters	$N_{\mathrm{Clusters}} \geq 80$
Number of TPC crossed rows	$N_{\mathrm{Rows,crossed}} \geq 70$
Ratio crossed rows	$N_{\mathrm{Rows,crossed}}/N_{\mathrm{Rows,findable}} \geq 0.83$
Cut shared clusters	True
Particle identification	$\lvert n_{\sigma,\mathrm{TPC,p}}\rvert < 3$ for $p_{\mathrm{TPC}} < 0.75$ GeV/c $n_{\sigma,\mathrm{comb,p}} < 3$ for $p_{\mathrm{TPC}} > 0.75$ GeV/c
Cut low p_{T} pions	Reject $\lvert n_{\sigma,\mathrm{TOF},\pi}\rvert < 3.0$ for $p_{\mathrm{TPC}} < 0.75$ GeV/c
Cut smallest n_{σ}	True

Table 4.2: Summary of proton track selections.

produced particles which are now travelling together as a jet. Such jets would include correlations present from the initial partons and therefore introduce an additional correlation between the formed hadrons. Due to the low relative momenta of the particle pairs within a jet, the measurement of the correlation function will include these correlations as well as a signal induced by the final state interaction. To reduce the contribution of the former, the events in this analysis are required to have a minimal sphericity of 0.7. In total 9.85×10^{8} events passed the event selection criteria without sphericity cut, and 5.34×10^{8} events with the applied selection of a minimum sphericity of 0.7.

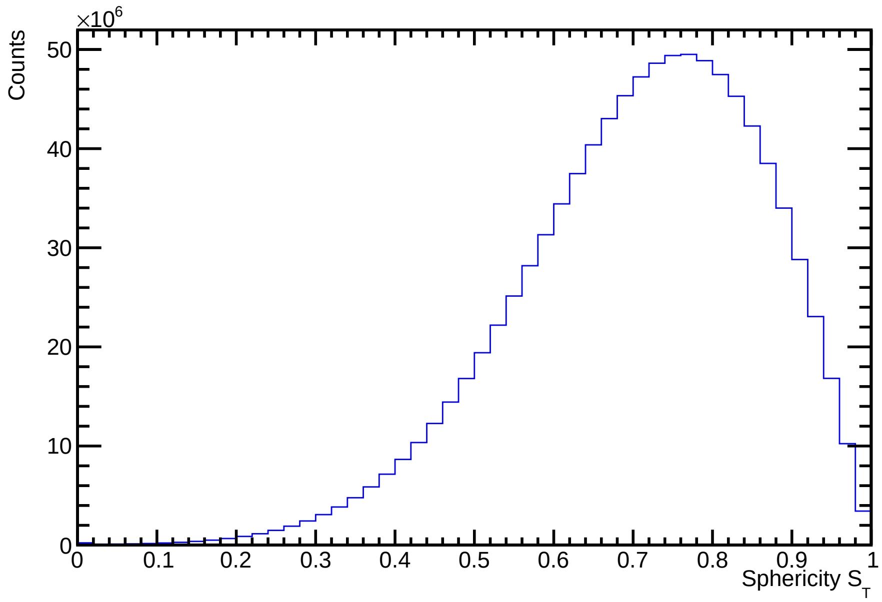

Figure 4.1: Sphericity distribution of events before selections.

4.2 Track selection

4.2.1 Proton selection

The track selections for protons are summarised in Table 4.2. The tracks are reconstructed using only the TPC information (so-called TPC only tracks, filter bit 128). The reconstructed transverse momentum is restricted to the range $0.5 < p_{\mathrm{T}} < 4.05$ GeV/c, as is shown in Fig. 4.2a.

A number of selections to the TPC information are made with the goal of removing fake tracks and achieving a high p_{T} resolution at large momenta. The tracks need to register at least 80 clusters in the TPC and cross at least 70 TPC rows to be accepted. Additionally, the track needs to register in at least 83% of the rows between the first and last row crossed in the TPC, the so-called findable rows. The distance of closest approach (DCA) of a track is the minimal distance between the track and the vertex position of its corresponding event. The DCA is restricted to minimise the influence of secondary tracks from long-lived weak decays, as well as those from other events entirely. The DCA must be smaller than 0.1 cm in the xy plane and 0.2 cm in the z direction. Additionally, the pseudorapidity is restricted to remove tracks at the edge of the detectors, which cover the pseudorapidity range $|\eta| < 0.9$, thereby rejecting tracks at the physical limit of the detectors whose reconstruction may be incomplete.

Particle identification is done using signals from the TPC and TOF detector. This is achieved by checking how many numbers of standard deviations n_σ the energy loss signal of the track is from the expected Bethe-Bloch curve (Fig. 3.5) of a specific particle type. For momenta below 0.75 GeV/c, the particle identification is done only by the TPC, where $|n_{\sigma,\mathrm{TPC,p}}|$ from the proton band must be smaller than 3.0. For larger momenta, as the bands start overlapping with each other and the band corresponding to a track becomes more difficult to discern, the TPC and TOF detectors are used in conjunction for particle identification. Here, the combined number of σ, defined as $n_{\sigma,\mathrm{comb,p}} = \sqrt{n^2_{\sigma,\mathrm{TPC,p}} + n^2_{\sigma,\mathrm{TOF,p}}}$, is required to be smaller than 3.

Finally, further selections are applied to minimise the number of misidentified particles. For momenta under 0.75 GeV/c, tracks are discarded if they have $|n_{\sigma,\mathrm{TOF},\pi}| < 3.0$, thus being likely to be pions instead of protons. For momenta above 0.75 GeV/c, tracks are rejected if their $n_{\sigma,\mathrm{comb}}$ is larger for protons than for another particle type: electrons, muons, pions, kaons, or deuterons.

4.2.2 Kaon selection

The track selections for kaons are summarised in Table 4.3. The accepted range for the transverse momentum of the kaon is $0.15 < p_{\mathrm{T}} < 2.0$ GeV/c, as is shown in Fig. 4.2b. The lower limit is applied to reject kaons stemming from primordial particles interacting with the material of the detector. The upper p_{T} cut is used to define a clear upper boundary used in the calculation of the fraction and purity while removing only a small amount of tracks.

Selections for track pseudorapidity and track DCA are kept the same as for the protons. The TPC must register at least 80 clusters per track, and each track must cross at least 70 rows, with a minimum of 80% of the rows being findable. For particle identification, two different methods are applied called *PID-1* and *PID-2*. In order for a track to be accepted as a kaon, the track has to pass at least one of the two methods. The method *PID-1* relies exclusively on PID information provided by the TPC and requires a PID signal $n_\sigma < 3.0$. It is used only for momenta $p < 0.85$ GeV/c. The momentum range $p \in [0.5, 0.65]$ GeV/c is excluded. To minimise contamination by pions and electrons, their n_σ is required to be larger than 3 in the momentum range $p \in [0.5, 0.85]$ GeV/c (for pions) and $p \in [0.3, 0.85]$ GeV/c (for electrons). The method *PID-2* uses combined PID information by the TPC and the TOF. In particular, the PID of kaons with $p > 0.85$ GeV/c is exclusively done with this method. It requires that $n_{\sigma,\mathrm{comb,K}} = \sqrt{n^2_{\sigma,\mathrm{TPC,K}} + n^2_{\sigma,\mathrm{TOF,K}}}$ is smaller than 3. Additionally, for $p > 1.2$ GeV/c, the tracks are rejected if $n_{\sigma,\mathrm{comb,K}} > 2$ or if $n_{\sigma,\mathrm{comb},\pi} < 6$. In this momentum range, due to the proximity of the kaon and pion curves in the TPC and TOF PID plots (see Fig. 3.5 and 3.6), these selections help clean up the kaon signal from possible misidentified pions.

Selection criteria	Value
Filterbit	128 (TPC only tracks)
Transverse momentum	$0.15 < p_{\mathrm{T}} < 2.0$ GeV/c
DCA vertex position	$\mathrm{DCA_{xy}} < 0.1$ cm $\mathrm{DCA_{z}} < 0.2$ cm
Pseudorapidity	$\lvert\eta\rvert < 0.8$
Number of TPC clusters	$N_{\mathrm{Clusters}} \geq 80$
Number of TPC crossed rows	$N_{\mathrm{Rows,crossed}} \geq 70$
Ratio crossed rows	$N_{\mathrm{Rows,crossed}}/N_{\mathrm{Rows,findable}} \geq 0.8$
Cut shared clusters	True
Particle identification	Method *PID-1* (TPC only): Kaon candidate excluded if: $p > 0.85$ GeV/c $n_{\sigma,TPC,K} > 3.0$ $p \in [0.5, 0.65]$ GeV/c $n_{\sigma,\mathrm{e}^{\pm}} < 3$ for $p \in [0.3, 0.85]$ GeV/c $n_{\sigma,\pi} < 3$ for $p \in [0.5, 0.85]$ GeV/c OR Method *PID-2* (TPC and TOF): Kaon candidate excluded if: $n_{\sigma,\mathrm{comb,K}} > 3$ for all momenta $n_{\sigma,\mathrm{comb,K}} > 2$ for $p_{\mathrm{TPC}} > 1.2$ GeV/c $n_{\sigma,\mathrm{comb},\pi} < 6$ for $p_{\mathrm{TPC}} > 1.2$ GeV/c
Cut smallest n_σ	True

Table 4.3: Summary of kaon track selections.

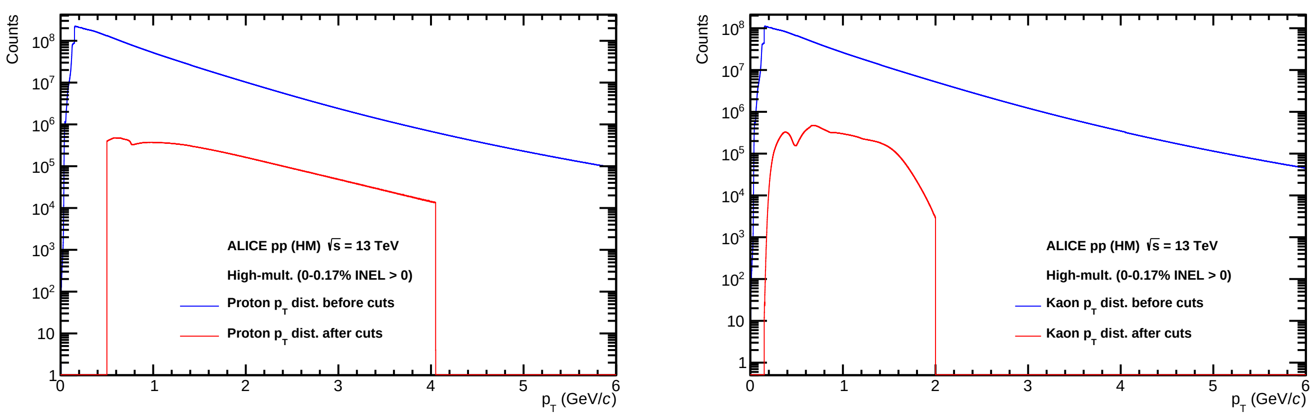

(a) p_{T} distribution of protons, before and after track selections.

(b) p_{T} distribution of kaons, before and after track selections.

Figure 4.2: p_{T} distributions for protons and kaons, before (blue) and after (red) track selection.

4.2.3 Selections on the pair level

In addition to the mentioned track selection, selections on the pair level have to be applied. In particular tracks that are close in space have to be removed, has they can be a result of a faulty reconstruction such as track merging or track splitting. The effect of this can be seen in the $\Delta\eta - \Delta\phi$ distributions of proton-kaon pairs in the same event in Fig. 4.3a. A clear deficiency of tracks with low $\Delta\eta - \Delta\phi$ can be seen. To remove this region, a elliptical $\Delta\eta - \Delta\phi$ is applied with values for the half-axis of $\Delta\eta = 0.017$ and $\Delta\phi = 0.04$. The result of this selection is shown in Fig. 4.3b. A similar selection is applied for the $\Delta\eta - \Delta\phi$ in the mixed event (Fig. 4.4) to guarantee an equal phase space compared to the same event.

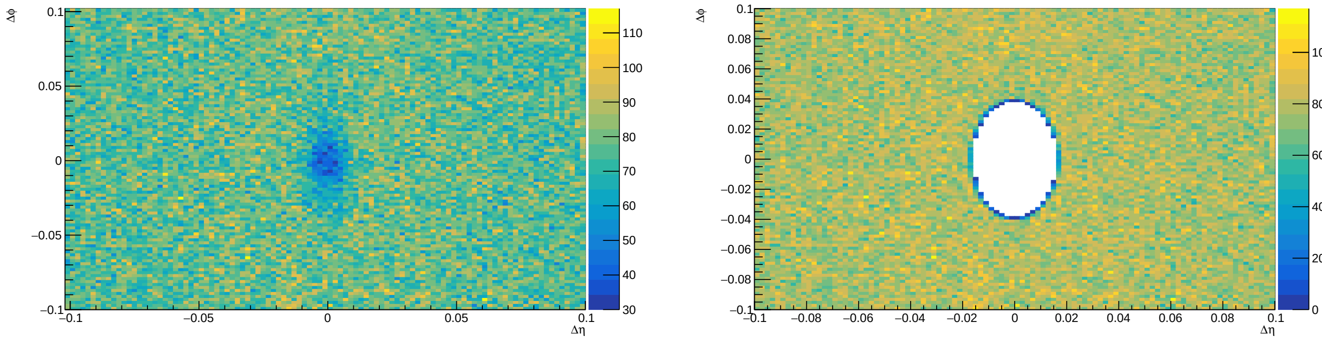

(a) $\Delta\eta - \Delta\phi$ of proton-kaon pairs in the same event before $\Delta\eta - \Delta\phi$ cut.

(b) $\Delta\eta - \Delta\phi$ of proton-kaon pairs in the same event after $\Delta\eta - \Delta\phi$ cut.

Figure 4.3: $\Delta\eta - \Delta\phi$ of proton-kaon pairs in the same event.

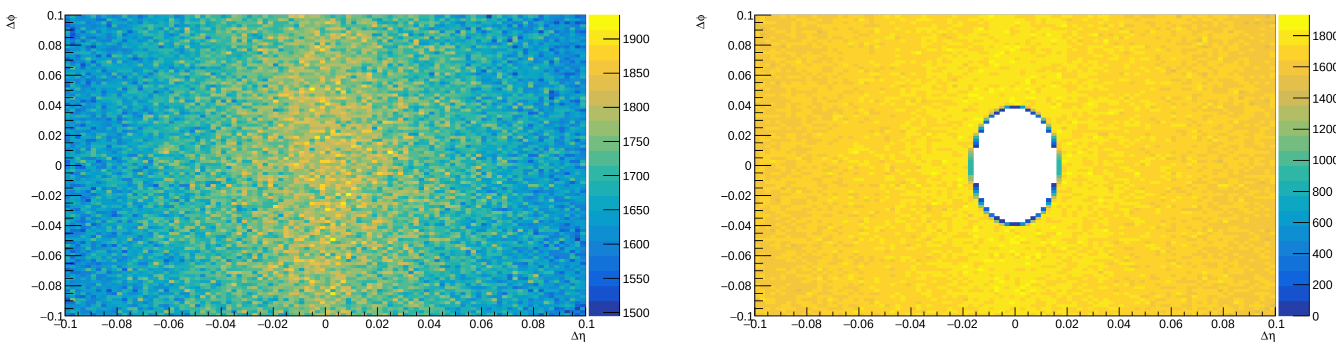

(a) $\Delta\eta - \Delta\phi$ of proton-kaon pairs in the mixed event before $\Delta\eta - \Delta\phi$ cut.

(b) $\Delta\eta - \Delta\phi$ of proton-kaon pairs in the mixed event after $\Delta\eta - \Delta\phi$ cut.

Figure 4.4: $\Delta\eta - \Delta\phi$ of proton-kaon pairs in the mixed event.

4.3 Experimental correlation functions and effects

This section discusses a few additional measures taken to improve the experimentally obtained correlation function. While some correlations are shown here already, the full discussion of the correlation functions is provided in Sec. 5.1.

4.3.1 Particle and anti-particle correlation functions

The strong and electromagnetic interactions are known to be invariant under the discrete charge conjugation transformation, hence the correlation functions for particles and for antiparticles should be equivalent. After applying the aforementioned event and track selections, the correlation function is evaluated for particle and antiparticle pairs separately by building the ratio of their respective same and mixed event distributions. A comparison for the exemplary $m_{\mathrm{T}} \in [1.0, 1.2)$ GeV/c bin is shown in Fig. 4.5. As can be seen, the correlation functions for particles and antiparticles are consistent within their statistical uncertainties. This observation also holds for all other m_{T} bins, respective figures are provided in App. A.1. Hence, in order to increase the statistics available for the correlation function, the relative momentum distributions obtained from particle and antiparticle pairs can be added together to form total same and mixed event distributions.

4.3.2 λ parameters

The same event distribution is subject to any sort of correlated particle pair which falls under the track selection criteria 4.2. This includes two key sources for particle pairs which should not contribute to the

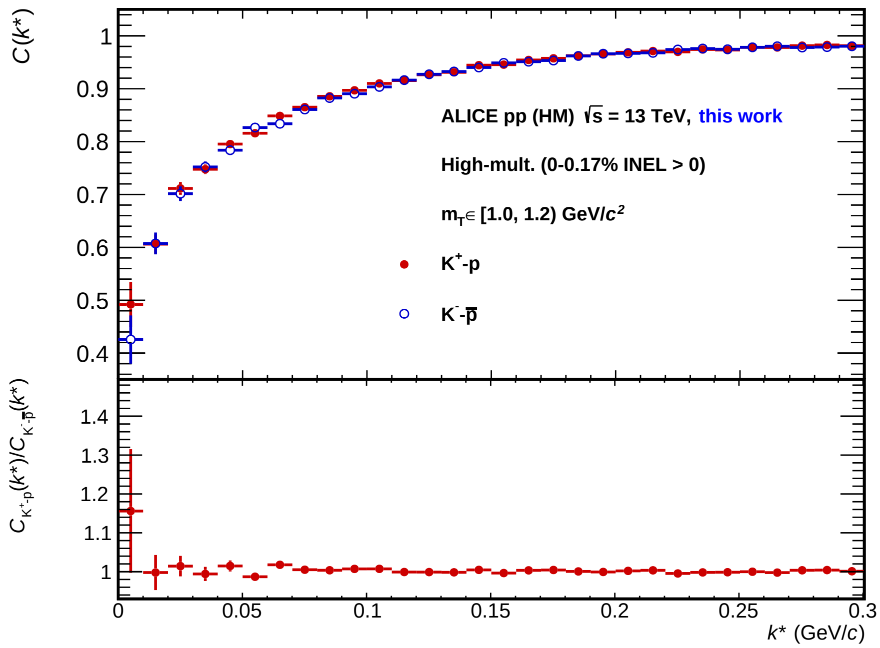

Figure 4.5: Ratio of particle to antiparticle correlation function for $1.0 < m_{\mathrm{T}} < 1.2$ GeV$/c^2$.

investigated correlation. Firstly, particles misidentified during particle identification should not contribute to the set of correctly identified particle pairs. Secondly, among the correctly identified pairs, there is feed-down from particles stemming from weak or electromagnetic decay channels, or from interactions with the detector material. These should also not be included when determining the correlation function as they may inherit the correlations of their mother particle, which is not the correlation that is to be examined [10].

Particle pairs from any of these channels will add up to create the same event distribution. This means that the correlation function is additive as well, and can be broken down into a component from the "genuine" pair, which is the pair of particles of interest, and contributions from each source of "non-genuine" pairs from feed-down and misidentification channels, each with their own weight. These statistical weights are known as λ parameters, which are calculated for each possible pair of particles that contribute to the correlation function. The λ parameter $\lambda_{ij} = P_i P_j f_i f_j$ for each particle pair i, j is composed of the purity P, which is the fraction of correctly identified particles, and the fraction f of particles produced by a specific channel compared to the overall particle yield. A consequence of their interpretation as statistical weights is that the sum $\sum_{ij} \lambda_{ij}$ adds up to 1.

Using these λ parameters, the effects of impurities and feed-down can be accounted for in the correlation function as

$$C(k^*) = 1 + \lambda_{\mathrm{genuine}} \cdot (C_{\mathrm{genuine}}(k^*) - 1) + \sum_{ij} \lambda_{ij} \left(C_{ij}(k^*) - 1\right) . \tag{4.1}$$

In the latter equation, $C_{\mathrm{genuine}}(k^*)$ represents the (theoretical) correlation function between genuine particle pairs while $C_{ij}(k^*)$ accounts for the correlation effects of the feed-down channels i, j and misidentified particles. In this analysis, the equation is simplified by assuming a flat correlation function for every feed-down channel, making the sum vanish and reducing Eq. (4.1) to

$$C(k^*) = \lambda_{\mathrm{genuine}} \cdot C_{\mathrm{genuine}}(k^*) + (1 - \lambda_{\mathrm{genuine}}) . \tag{4.2}$$

4.3.3 Non-femtoscopic background

Outside of the range of the interaction, the effects of the interaction are no longer felt by the particles and the correlation function is expected to approach unity. However, the correlation function obtained from data may exhibit deviations from unity due to non-femtoscopic background effects, which modify the correlation function also within the femtoscopic range [45]. To account for this, the measured correlation function from Eq. (4.2) is multiplied by an additional background function $C_{\mathrm{bkg}}(k^*)$. By doing so, the overall correlation function can accommodate a background signal outside of the femtoscopic region, where the measured correlation function is expected to go to unity if there were no additional signal. The shape taken by the background function in the non-femtoscopic region can then be propagated to low k^* values to obtain an estimate for the background shape in the femtoscopic signal region.

In this analysis, a third order polynomial without a linear term is chosen to model the background

$$C_{\mathrm{bkg}}(k^*) = \mathcal{N} \cdot (1 + a \cdot k^{*2} + b \cdot k^{*3})\,. \tag{4.3}$$

Here, $\mathcal{N}$, a and b are free parameters determined by fitting $C_{\mathrm{bkg}}(k^*)$ to the correlation function outside the femtoscopic region. The resulting function is then multiplied to Eq. 4.2, with $\mathcal{N}$ set to 1 (as the function is renormalised by the total fit) and the other parameters kept constant, to model the total correlation function which is fitted to experimental data.

4.3.4 Momentum resolution

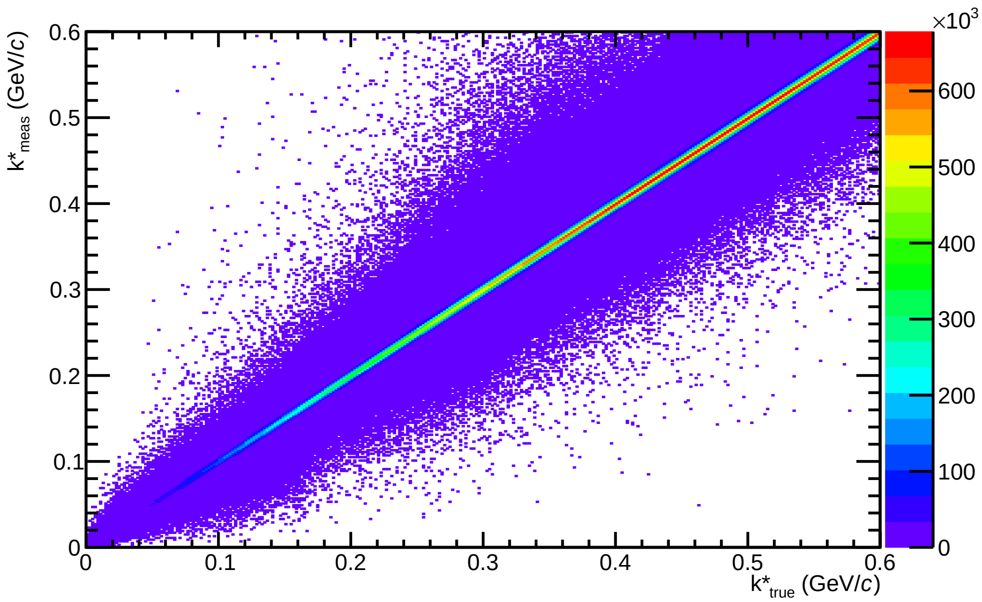

Figure 4.6: Momentum smearing matrix, determined by Monte Carlo simulations.

Any detector used for reconstructing tracks will have a finite resolution, and the measured relative momentum k^*_{meas} will deviate from the true relative momentum k^*_{true} of the particle pair. This is compensated in the calculation of the theoretical correlation function through the use of a momentum smearing matrix $M(k^*_{\mathrm{true}}, k^*_{\mathrm{meas}})$, shown in Fig. 4.6. This is obtained from Monte Carlo simulations (Sec. 3.4) and indicates the distribution of k^*_{meas} values for a given k^*_{true} generated in the simulation. The correlation function is then adapted by calculating the integral

$$C(k^*_{\mathrm{meas}}) = \int_0^\infty M(k^*_{\mathrm{true}}, k^*_{\mathrm{meas}}) \cdot C(k^*_{\mathrm{true}})\,\mathrm{d}k^*_{\mathrm{true}}\,. \tag{4.4}$$

4.3.5 Multiplicity reweighting

Another step in correcting the correlation function is multiplicity reweighting. This relates to the fact that certain multiplicity bins might not be equally probable in the mixed event sample compared to the same

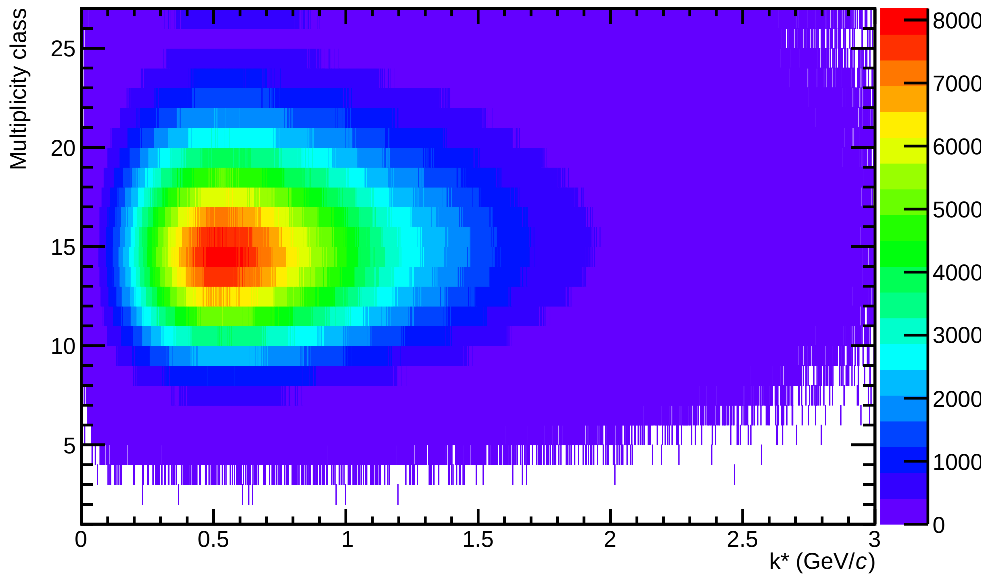

Figure 4.7: k^* distribution versus multiplicity class for $(1.2 < m_{\mathrm{T}} < 1.4)$ GeV/c^2.

events sample. To account for this, the same and mixed event momenta distributions are sorted into a different bins (classes) based on their event multiplicity, as it can be seen in Fig. 4.7. The multiplicity bins for this analysis are chosen as $[0, 4)$, $[4, 8)$, $[8, 12)$, ... $[100, \infty)$. Using this, a projection is made into each multiplicity class to get multiplicity differential momentum distributions. Each of the same and mixed event distributions of a specific multiplicity bin are weighted with the fraction of same event pairs in this multiplicity bin, divided by the total same event yield. In this way, the mixed event is effectively reweighted to the multiplicity of the same event (see Fig. 4.8). Adding together the distributions for each multiplicity bin produces the multiplicity-reweighted same and mixed event momentum distributions. The ratio of the unweighted correlation function to the multiplicity reweighted correlation function is shown in Fig. 4.9 for the example $m_{\mathrm{T}} \in [1.0, 1.2)$ GeV/c. Deviations between the two correlation functions can only be seen for very large relative momenta. For low k^* they agree with each other within their statistical uncertainties. Equivalent comparisons plots for reweighted and non-reweighted correlation functions for all m_{T} bins can be found in App. A.2 yielding the same observation as in Fig. 4.9.

4.4 Determination of λ parameters

The λ parameters, which account for particles that were misidentified or are feed-downs from weak or electromagnetic decays, are determined in a data-driven approach. The experimental data of the track DCA is fitted with templates of the DCA distributions for different production channels of protons and kaons. These include primary and secondary particles, as well as particles stemming from interactions with the detector material. These templates are derived from the Pythia8.2 and GEANT3 MC simulations [41, 42]. The fitting procedure is performed for 20 equally partitioned p_{T} bins, where within each bin the templates are fitted to the experimental data to extract the various feed-down fractions the particle yield is composed of. Example fits for both protons and kaons are shown in 4.10. The purities of protons (kaons) are obtained with MC events by comparing the p_{T} distribution of the identified particles to the p_{T} distribution of identified particles, where in addition the particle identity was checked with the available MC information.

The fractions and purities are shown in Figs. 4.11 and 4.12. For protons, the feed-down contributions considered are from Λ and Σ^+ particles, which are both decay into protons through the weak interaction, and account for 9.5% and 3.8% of the proton yield respectively. Protons produced from interactions with detector material account for 0.5% on average. For kaons, the sources of secondary particles are not calculated

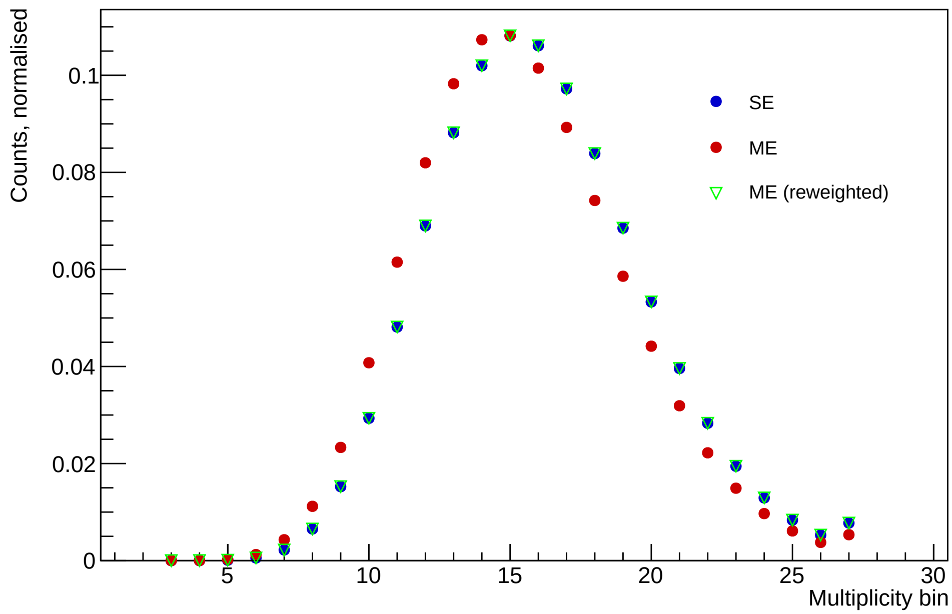

Figure 4.8: Multiplicity bin distribution (normalised counts) of the same event, mixed event and mixed event multiplicity reweighted for $1.2 < m_{\mathrm{T}} < 1.4$ GeV$/c^2$.

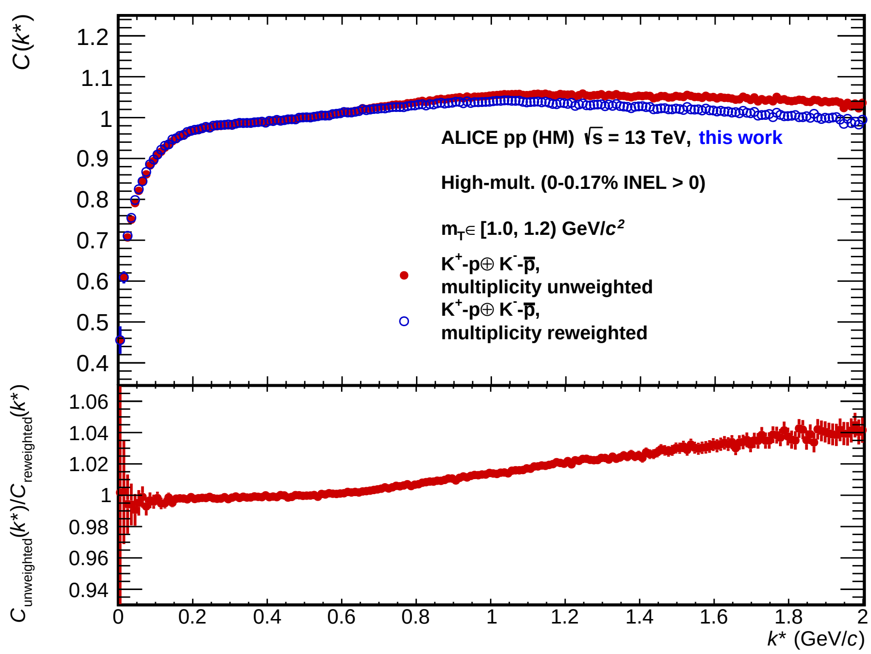

Figure 4.9: Ratio of unweighted to multiplicity reweighted correlation function for $(1.0 < m_{\mathrm{T}} < 1.2)$ GeV$/c^2$.

differentially, and account for only 0.6% in the DCA fit. However, the contributions of kaons from ϕ mesons, which are not included in the DCA fit, produce 5.99% of kaons, so the primary fraction needs to be scaled accordingly by 94.01%. The p_{T}-averaged purity of protons (kaons) is found to be very high at 98.4% (98.1%).

In most femtoscopic analyses, the λ parameter is calculated by averaging the fractions and purities for

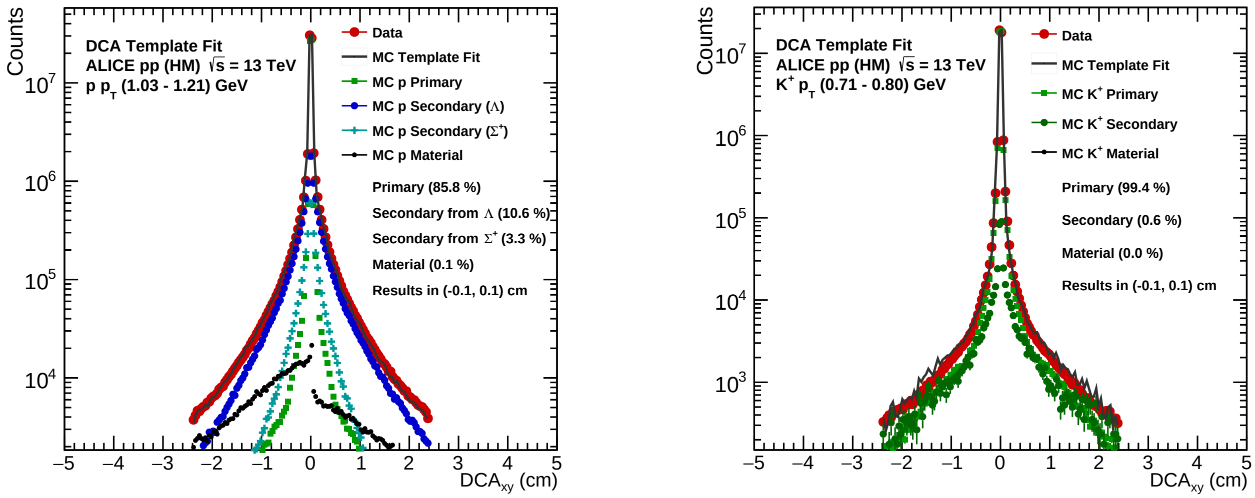

(a) Proton DCA fit for $1.03 < p_{\mathrm{T}} < 1.21$ GeV/c.

(b) Kaon DCA fit for $0.71 < p_{\mathrm{T}} < 0.80$ GeV/c.

Figure 4.10: Example DCA fits for proton and kaon data.

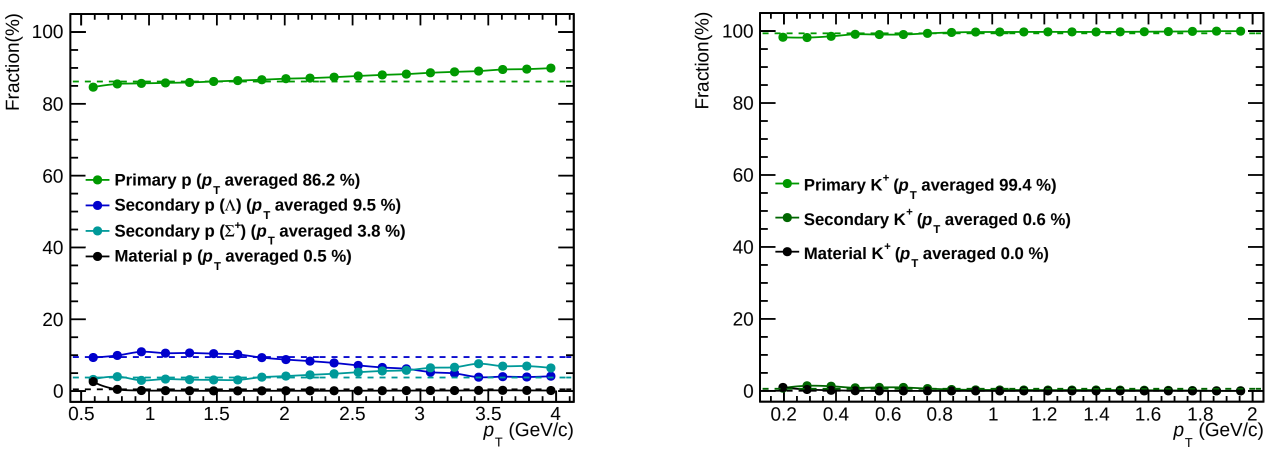

(a) Fractions for protons.

(b) Fractions for kaons.

Figure 4.11: Fractions for protons and kaons in the p_{T} ranges (0.5 - 4.05) GeV/c and (0.15 - 2.0) GeV/c, respectively.

both particle species over the full p_{T} range independently. They are then multiplied together to create one genuine λ parameter, $\lambda_{\mathrm{gen}} = P_p P_K f_p f_K$, that covers all transverse mass bins. This "traditional" method leads to a $\lambda_{\mathrm{traditional,\,gen}}$ of 0.776. However, what is neglected by this method is the underlying distribution of p_{T} within each m_{T} bin, as not every bin will contain the full p_{T} spectrum. Additionally, the method also does not consider any correlation between the p_{T} of the protons and kaons. These issues are addressed in a new method for calculating λ parameters m_{T}-differentially and will be outlined here.

For every m_{T} bin, a two-dimensional histogram is filled with the p_{T} values of every proton-kaon pair in the experimental data with $k^* < 200$ MeV/c, as shown in Fig. 4.13. In this way, only pairs which are relevant for the femtoscopic region are taken into account. This histogram acts as a map $M(p_{\mathrm{T,p}}, p_{\mathrm{T,K}})$, showing how the transverse momentum of the two particles are correlated. The overall λ parameter for that m_{T} bin is calculated by integrating the fractions and purities of both particle species, obtained as a

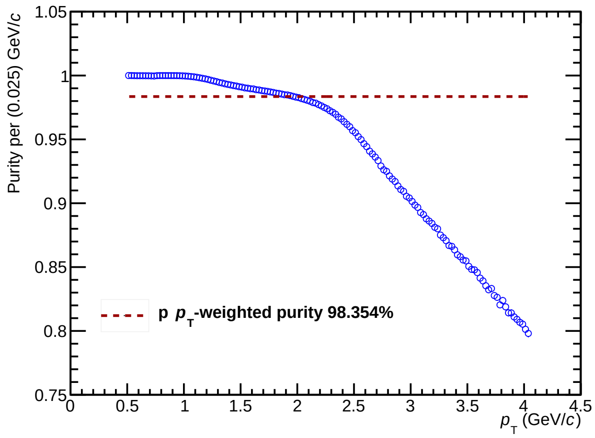

(a) Purities for protons.

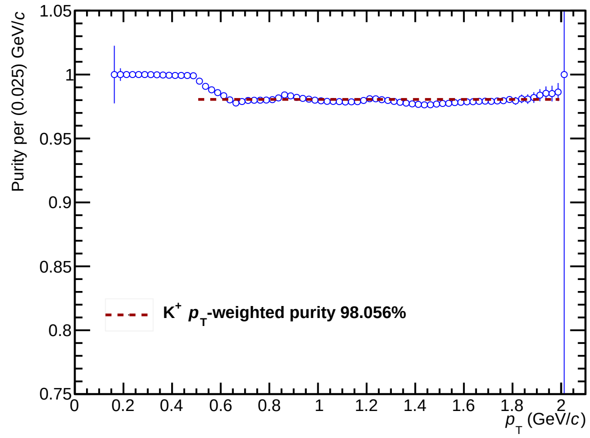

(b) Purities for kaons.

Figure 4.12: Purities for protons and kaons in the p_{T} ranges (0.5 - 4.05) GeV/c and (0.15 - 2.0) GeV/c, respectively.

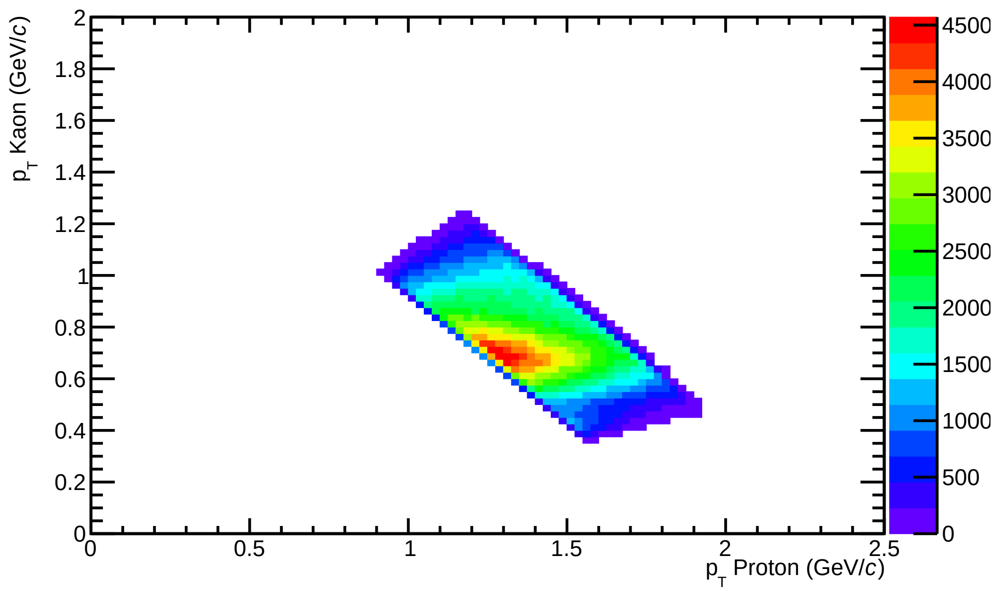

Figure 4.13: p_{T} of protons versus p_{T} of kaons for $(1.2 < m_{\mathrm{T}} < 1.4)$ GeV/c, $k^* < 200$ MeV/c.

function of p_{T} from the DCA fits, over this map. By doing so, the integrand is weighted by the $p_{\mathrm{T,p}}$-$p_{\mathrm{T,K}}$ distribution, leading to the overall expression

$$\lambda = N \cdot \iint M(p_{\mathrm{T,p}}, p_{\mathrm{T,K}}) \cdot f_p(p_{\mathrm{T,p}}) \cdot f_K(p_{\mathrm{T,K}}) \cdot P_p(p_{\mathrm{T,p}}) \cdot P_K(p_{\mathrm{T,K}})\, \mathrm{d}^2 p_{\mathrm{T,p}} p_{\mathrm{T,K}}\,, \tag{4.5}$$

where N is the normalisation factor of the map $N = 1/\iint M(p_{\mathrm{T,p}}, p_{\mathrm{T,K}})\, \mathrm{d}^2 p_{\mathrm{T,p}} p_{\mathrm{T,K}}$. However, the map $M(p_{\mathrm{T,p}}, p_{\mathrm{T,K}})$ is not continuous but consists of equally sized bins for the proton and kaon transverse momenta. Due to this finite p_{T} bin size of the map, as well as the fraction and purity functions, Eq. (4.5) needs to be modified. For every $p_{\mathrm{T,p}}$-$p_{\mathrm{T,K}}$ bin of $M(p_{\mathrm{T,p}}, p_{\mathrm{T,K}})$, a linear interpolation is made between the closest p_{T} bins for the fractions and purities from Fig. 4.11 and 4.12 respectively. The λ parameter is then calculated as a sum rather than an integral, hence Eq. (4.5) becomes

$$\lambda = N_{finite} \cdot \sum_{p_{\mathrm{T,p}}, p_{\mathrm{T,K}}} M(p_{\mathrm{T,p}}, p_{\mathrm{T,K}}) \cdot f_p(p_{\mathrm{T,p}}) \cdot f_K(p_{\mathrm{T,K}}) \cdot P_p(p_{\mathrm{T,p}}) \cdot P_K(p_{\mathrm{T,K}})\,. \tag{4.6}$$

The parameter N_{finite} represents again the proper normalisation factor of the map $N_{finite} = 1/\sum_{p_{\mathrm{T,p}}, p_{\mathrm{T,K}}} M(p_{\mathrm{T,p}}, p_{\mathrm{T,K}})$. This results in λ parameters that differ from bin to bin, as shown in Fig. 4.14. Only a very weak dependence of the λ-parameter on m_{T} can be observed. In particular, the first 5 m_{T} bins vary by less than one per-cent, will the difference between the first and last bin is of about one per-cent. The obtained values in the m_{T}-differential way are also consistent with the "traditional" $\lambda_{\text{traditional, gen}}$ of 0.776. Nonetheless, the new m_{T}-differential λ parameters are used for the further analysis.

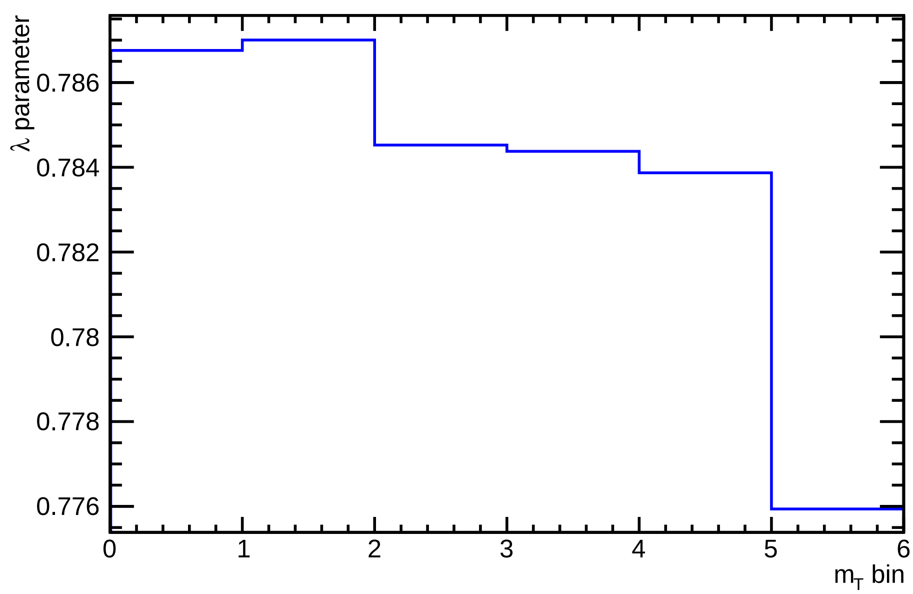

Figure 4.14: λ parameters for each of the six m_{T} bins.

4.5 Systematic variations

There are two sources of uncertainty for the experimental correlation functions, statistical and systematic. Statistical uncertainties are due to random fluctuations in the dataset, arising from the fact that no two events will be completely identical, and the measured values are subject to some level of intrinsic randomness. This variation is minimised by increasing the sample size of the analysed dataset. On the other hand, systematic uncertainties arise from potential biases in the methodology used to obtain and process the data. They should provide an estimate as to how confident one is that the methodology used in the analysis provides the correct result.

In this analysis, the systematic uncertainties of the correlation functions have been obtained through the method of systematic variations. The values used for the proton and kaon track selections in Tab. 4.2 and 4.3 are varied as shown in Tab. 4.4. Additionally, the $\Delta\eta - \Delta\phi$ cut on the pair level is varied by $\Delta\eta \pm 0.002$ and $\Delta\phi \pm 0.005$. In total 44 systematic varitions have been created by randomly combining the varied selections shown in Tab. 4.4 together with the $\Delta\eta - \Delta\phi$ cut. In this way, any correlations between the variations are taken into account. For each of the 44 systematic variations the correlation function is obtained in each m_{T} bin. Only systematic variations which differ by less than 10 % in the same event yield for $k^* < 200$ MeV/c are taken into account. In this way, differences due to statistical fluctuations are minimised. Exception to this is the first bin $m_{\mathrm{T}} \in [0.0, 1.0)$ GeV/c^2 where up to 30% are allowed, otherwise almost no systematic variation would pass this selection. The difference between each systematically varied correlation function and the default correlation function in each k^* bin is shown in Fig. 4.15 with the example of the last m_{T} bin. The maximal positive and negative difference in values for each k^* bin is taken as the spread of the systematic variations. Under the assumption that the spread of the systematic variations is uniform across the end points a and b of the spread, the systematic uncertainty is calculated as

$$\sigma_{\mathrm{syst}} = \frac{|b-a|}{\sqrt{12}} \,. \tag{4.7}$$

The systematic uncertainties relativ to the default correlation function are shown in Fig. 4.16. The systematic uncertainty is the largest for the low k^* region, with up 2.5% for the first and second m_{T} bin, up to 5% for the third, fourth and fith, and up to 18% for the last m_{T} bin.

Variable	Default	Variation
p_{T} Proton (GeV/c)	0.5	0.4, 0.6
$\|\eta\|$ Proton	0.8	0.77, 0.83
n_{Cluster} Proton	80	70, 90
n_{σ} Proton	3	2.5, 3.5
p_{T} Kaon (GeV/c)	0.15	0.1, 0.2
$\|\eta\|$ Kaon	0.8	0.75, 0.85
n_{Cluster} Kaon	80	70, 90
$n_{\sigma,\mathrm{TPC}}$ Kaon	3	2.7, 3.3
$n_{\sigma,\mathrm{comb}}$ Kaon	3	2.7, 3.3
$n_{\sigma,\mathrm{exclusion}}$ Kaon	3	3.3, 2.7

Table 4.4: Summary of track selection variations.

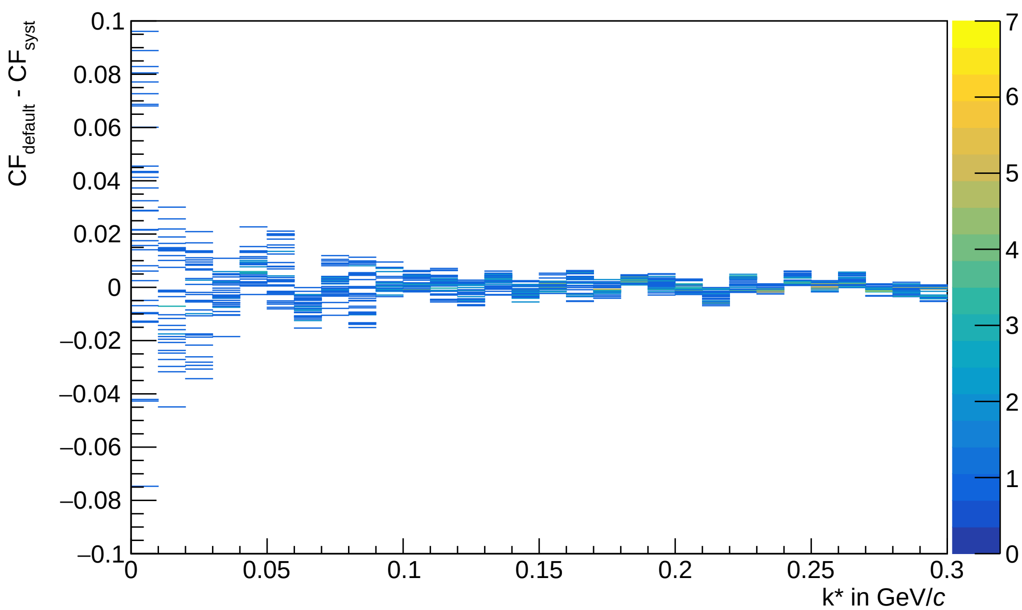

Figure 4.15: Difference between default and systematic correlation functions for $m_{\mathrm{T}} \in [1.8, 2.0)$ GeV/c^2.

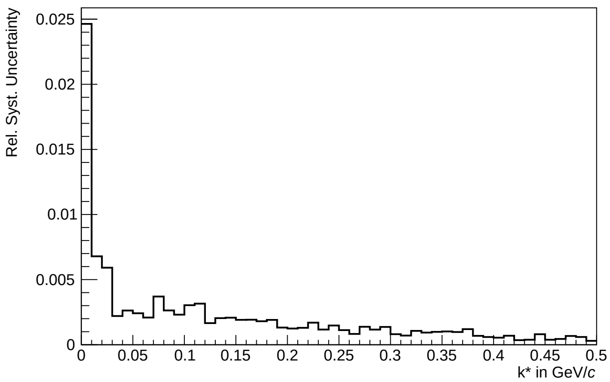

(a) $m_{\mathrm{T}} \in [0.7, 1.0)$ GeV/c^2

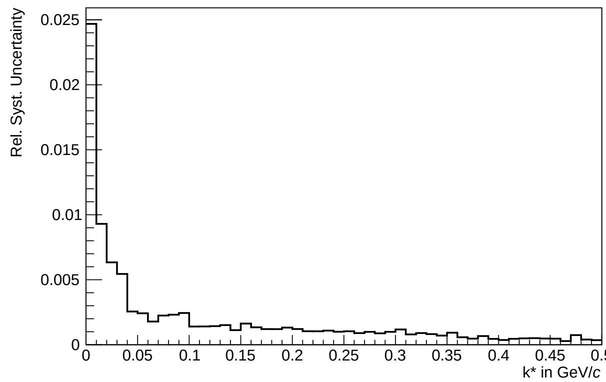

(b) $m_{\mathrm{T}} \in [1.0, 1.2)$ GeV/c^2

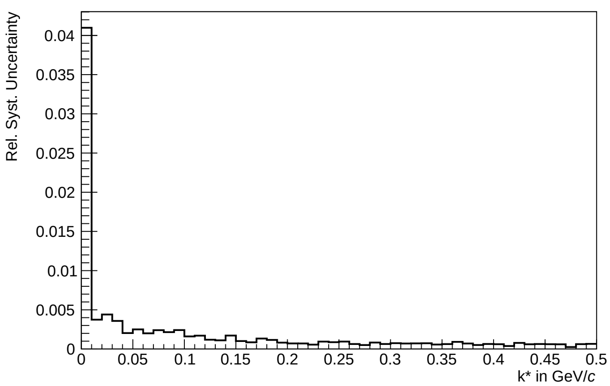

(c) $m_{\mathrm{T}} \in [1.2, 1.4)$ GeV/c^2

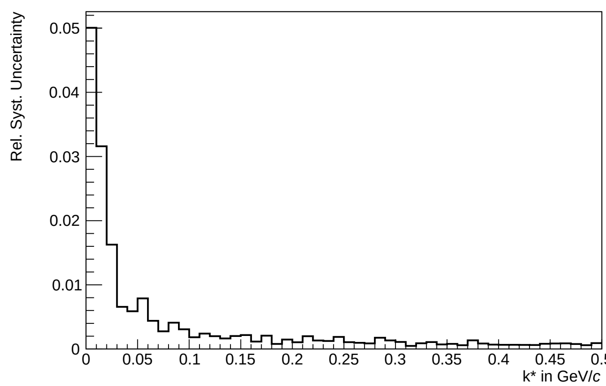

(d) $m_{\mathrm{T}} \in [1.4, 1.5)$ GeV/c^2

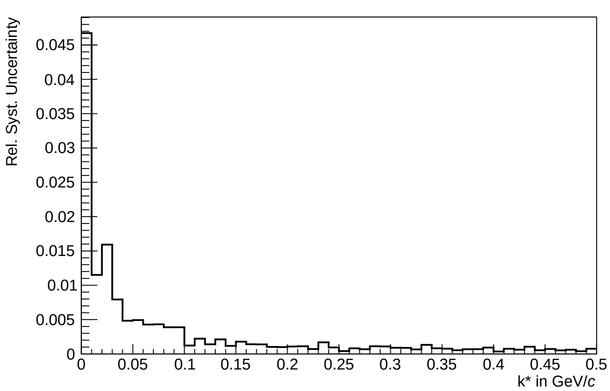

(e) $m_{\mathrm{T}} \in [1.5, 1.8)$ GeV/c^2

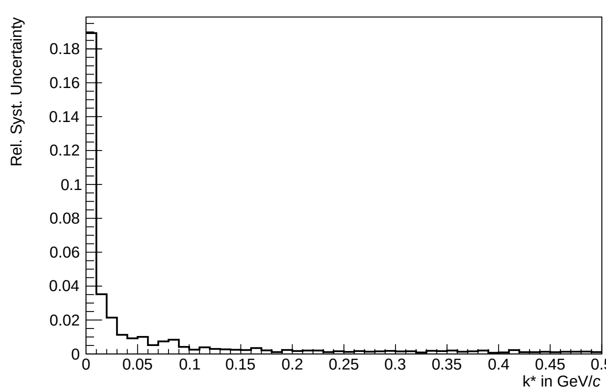

(f) $m_{\mathrm{T}} \in [1.8, 2.0)$ GeV/c^2

Figure 4.16: Systematic uncertainties relative to the default correlation function for each m_{T} bin.

Chapter 5

Results and Discussion

5.1 Proton-Kaon correlation functions

Using the mentioned event and track selection criteria, the correlation function of the K^+p systems are evaluated for six different m_T bins. Table 5.1 shows the amount of pairs for each m_T in the femtoscopic relevant region of $k^* < 200$ MeV/c. The multiplicity reweighted correlation functions are shown with their statistical and systematic uncertainties in Fig. 5.1. These functions are normalised in the range $k^* \in [400, 600]$ MeV/c. The bin centers have been shifted according the centre of gravity of the underlying mixed event k^* distribution in each bin. This shifted is accordingly applied in all figures presented in this chapter. The correlation function is below unity in the low k^* range, as expected for the repulsive interaction between protons and kaons. Beyond this range, the femtoscopic signal diminishes and the shape of the correlation function is dominated by background effects. In the next sections, these correlation function are fitted using the two different available source models, the RSM and the CECA.

m_T range in GeV/c^2	Counts K^+p	Counts $K^-\bar{p}$
$[0.7, 1.0)$	2.32×10^6	1.87×10^6
$[1.0, 1.2)$	1.67×10^6	1.27×10^6
$[1.2, 1.4)$	0.99×10^6	0.78×10^6
$[1.4, 1.5)$	0.31×10^6	0.25×10^6
$[1.5, 1.8)$	0.48×10^6	0.40×10^6
$[1.8, 2.0)$	0.13×10^6	0.11×10^6

Table 5.1: Counts of pairs $K^+ - p$ and anti-pairs $K^- - \bar{p}$ for each m_T bin in the femtoscopic relevant region of $k^* < 200$ MeV/c.

5.2 Results from RSM

The first source model which is tested on the experimental K^+p correlation functions is the RSM. The first step is building the source function. As described in Sec. 2.2.2, the source is constructed from the different combinations of proton and kaon primordials and resonances. The core source of primordial pairs is modelled by a Gaussian distribution. For the effect of short-lived resonances, the effective resonances with the masses and lifetimes is used. The probability for the proton or kaon to originate from the decay of their effective resonance is 64% and 48%, respectively. After the construction of the source, the only free parameter of the source function is the core source size r_{core}.

The correlation function of the K^+-p system is evaluated within the RSM using the CATS framework. In the first step the Schrödinger equation is solved by CATS assuming χEFT [26, 25] (Sec. 2.2.3) for the particle interaction. In the second step, the convolution of the source and wave function, as described by Eq. (2.3), is evaluated by CATS to produce the correlation function. The source used for the calculation of the Koonin-Pratt equation is constructed with the RSM approach, in which the non-Gaussian contributions to the source are modelled via a dedicated MC procedure (see Sec. 3.4).

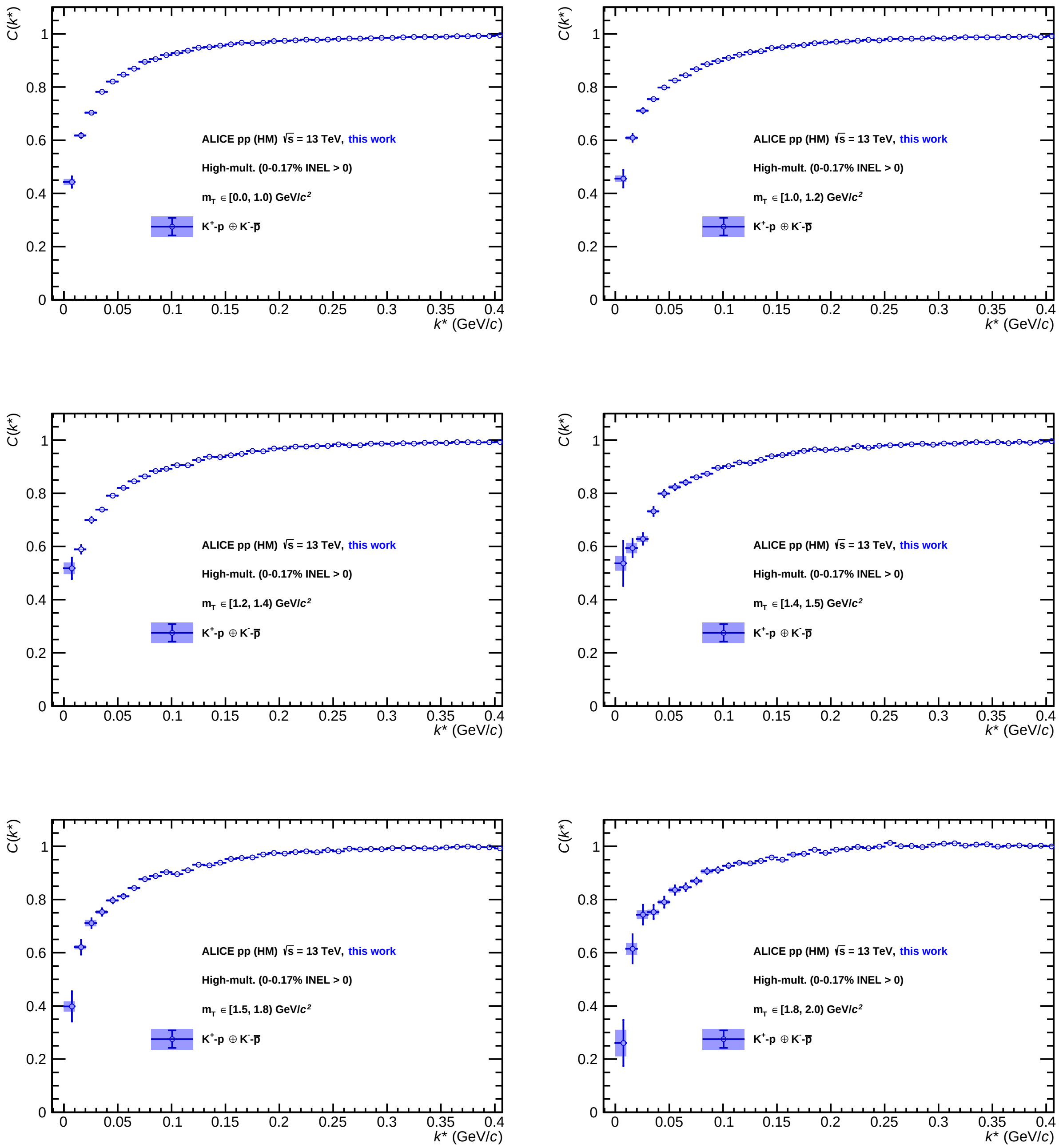

Figure 5.1: The correlation functions obtained in every m_{T} bin. The statistical uncertainties are given as lines and the systematic uncertainties are given as the shaded boxes.

The experimental correlation function is first fitted with the background function from Eq. (4.3) in the range $k^* \in [275, 600]$ MeV/c. This region is chosen for the pre-fit as the shape of the background effects is well constrained by the third order polynomial in this range. This allows for an extrapolation of the background to the low k^* region, as shown in Fig. 5.2 for the example of $m_{\mathrm{T}} \in [1.2, 1.4)$ GeV/c^2. The corresponding pre-fits of all other m_{T} bins are shown in App. B.1 The overall correlation function, which is fitted to the data in the momentum region $k^* \in [0, 400]$ MeV/c, is

$$C(k^*) = \mathcal{N} \cdot (1 + a \cdot k^{*2} + b \cdot k^{*3}) \cdot [\lambda_{\mathrm{genuine}} \cdot C_{\mathrm{genuine}}(k^*) + (1 - \lambda_{\mathrm{genuine}})] \ . \tag{5.1}$$

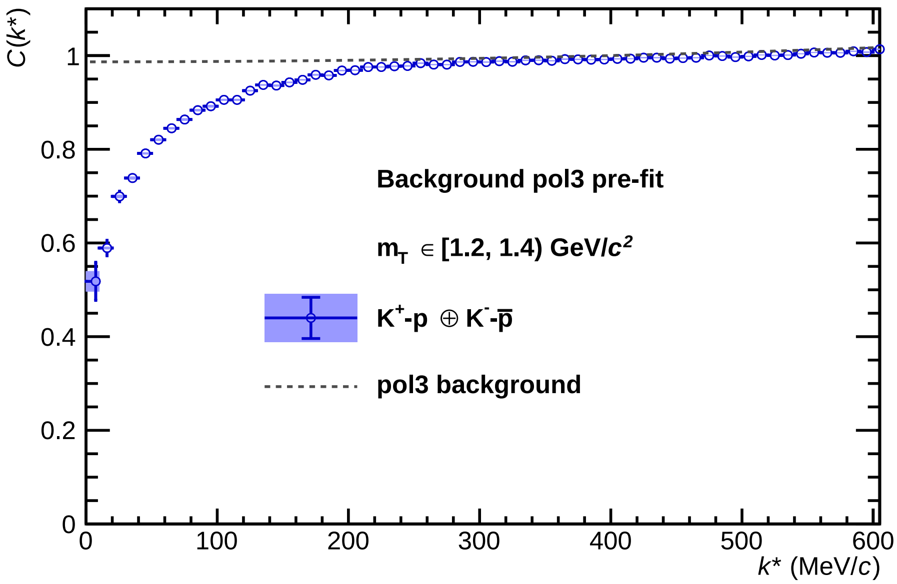

Figure 5.2: Polynomial pre-fit for the $1.2 < m_{\mathrm{T}} < 1.4$ GeV$/c^2$ bin, shown by the dashed grey line. The pre-fit is performed in the range $k^* \in [275, 600]$ MeV$/c$ and then extrapolated to the low k^* region.

This range is chosen as it focuses on the femtoscopic region, where the shape of the correlation function is most heavily modified due to the interaction. As such, the correlation function obtained through the fitting procedure is sensitive to the r_{core}, allowing for proper extraction of the core source size. The $\lambda_{\mathrm{genuine}}$ parameters are those obtained in Sec. 4.4.

As the interaction model and background have been fixed, the only two fit parameters are the normalisation $\mathcal{N}$ and core source size r_{core}, the latter of which is included in $C_{\mathrm{genuine}}(k^*)$. The results of the fit for every m_{T} bin are shown in Fig. 5.3. The solid green line shows the total fit function (Eq. (5.1)), which is determined by the resonance source model and χEFT interaction. In the first k^* bin, the momentum smearing of the theoretical fit function results in a diminished correlation strength at that point due to the asymmetry of the k^*_{meas} distribution, as k^*_{true} must be positive. With the exception of this k^* bin, the function describes the experimentally obtained data points well, shown in blue. The red lines in Fig. 5.3 represent the correlation functions evaluated for a Coulomb-only interaction using the same source function as for the χEFT interaction. These lie significantly above the data points in the range $k^* \in [30, 200]$ MeV$/c$, demonstrating the importance of the strong interaction in the K$^+$-p system. The latter leads to an amplification of the correlation between the particles beyond the k^* region dominated by Coulomb effects.

To quantify the goodness of each fit, the χ^2/NDF value is calculated for the overall correlation function in each m_{T} bin. For a fit function $CF_{fit}(k^*)$, its χ^2 is defined as

$$\chi^2 = \sum_{i=1}^{N} \frac{(CF_{exp.}(k_i^*) - CF_{fit}(k_i^*))^2}{\sigma_i^2} \,. \tag{5.2}$$

At every data point $(k_i^*, CF_{exp.}(k_i^*))$ of the experimental data, the difference between the point and the fit function, calculated at k_i^*, is squared and then divided by the squared uncertainty σ_i^2 of the data point. Here, σ_i^2 is the combined uncertainty consisting of statistical and systematic uncertainties defined as $\sigma_i^2 = \sigma_{stat.,i}^2 + \sigma_{syst.,i}^2$ .The larger the difference between fit and experimental data, the greater the contribution to the χ^2, indicating a poorer overall fit. Finally, the χ^2 is divided by the number of degrees of freedom (NDF), which is the number of data points N minus the number of fit parameters (NDF = 40 - 2 in this case). The χ^2/NDF values evaluated for each m_{T} bin are shown in Fig. 5.4, the largest of which is

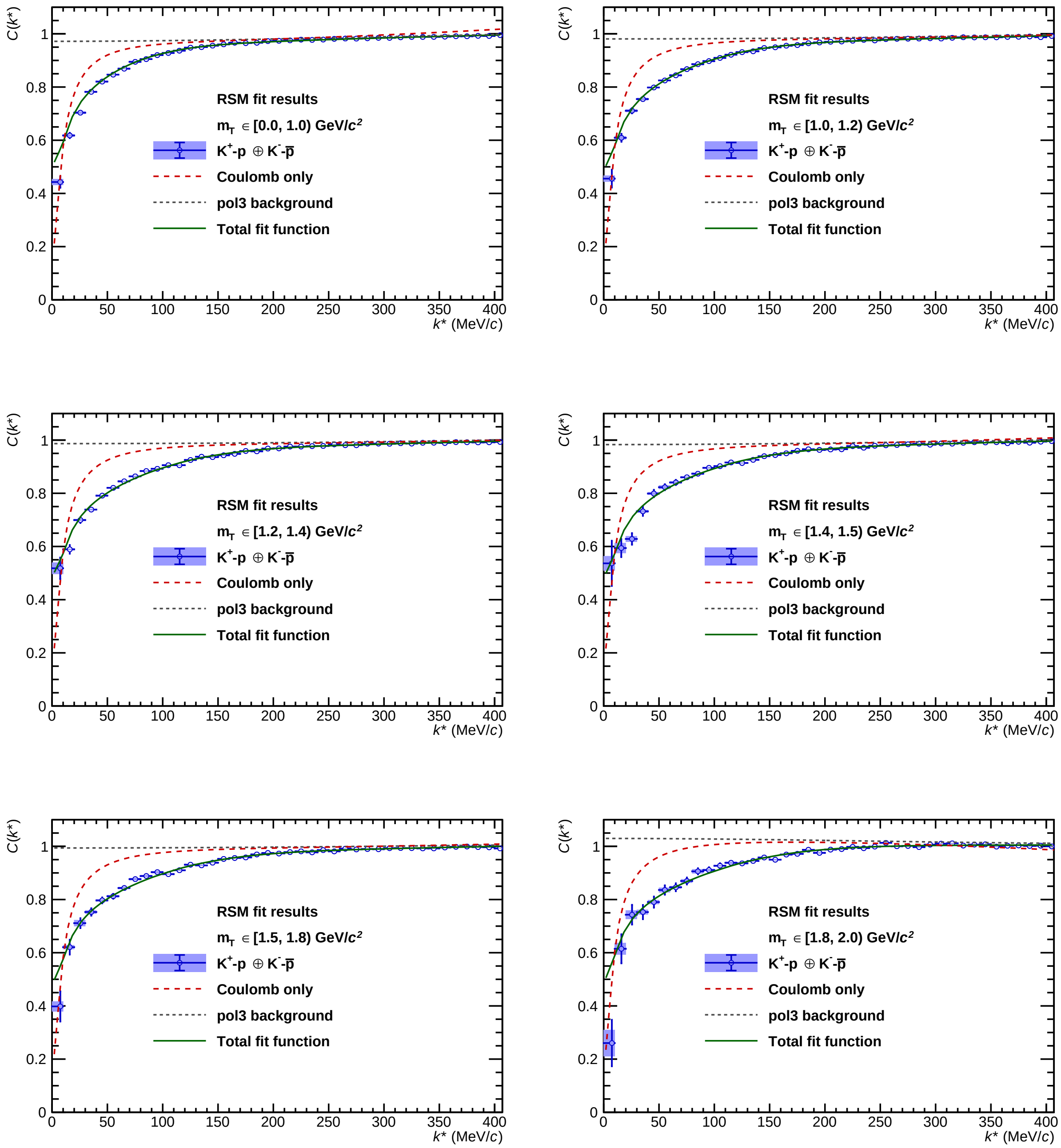

Figure 5.3: The fit results for the RSM in each m_{T} bin. The experimental correlation functions, with statistical (lines) and systematic (shaded boxes) uncertainties, are shown in blue. The polynomial pre-fit, extrapolated to low k^* values, is given by the grey dashed line. The correlation functions, calculated for the Coulomb + strong interaction and Coulomb-only interaction with the same source function, are given by the solid green and dashed red line, respectively.

that in the first bin with a χ^2/NDF of about 2.8, demonstrating that the fits perform well in all m_{T} bins.

The statistical uncertainties for the extracted r_{core} values from the RSM fit are determined by including only statistical uncertainties in the data points, rather than the combined statistical and systematic uncertainty. To determine the systematic uncertainties for these values, the fitting procedure is performed for each of the variations listed in Tab. 5.2. The difference $\Delta r_{\mathrm{core}} = r_{\mathrm{core,default}} - r_{\mathrm{core,var}}$ between the radii

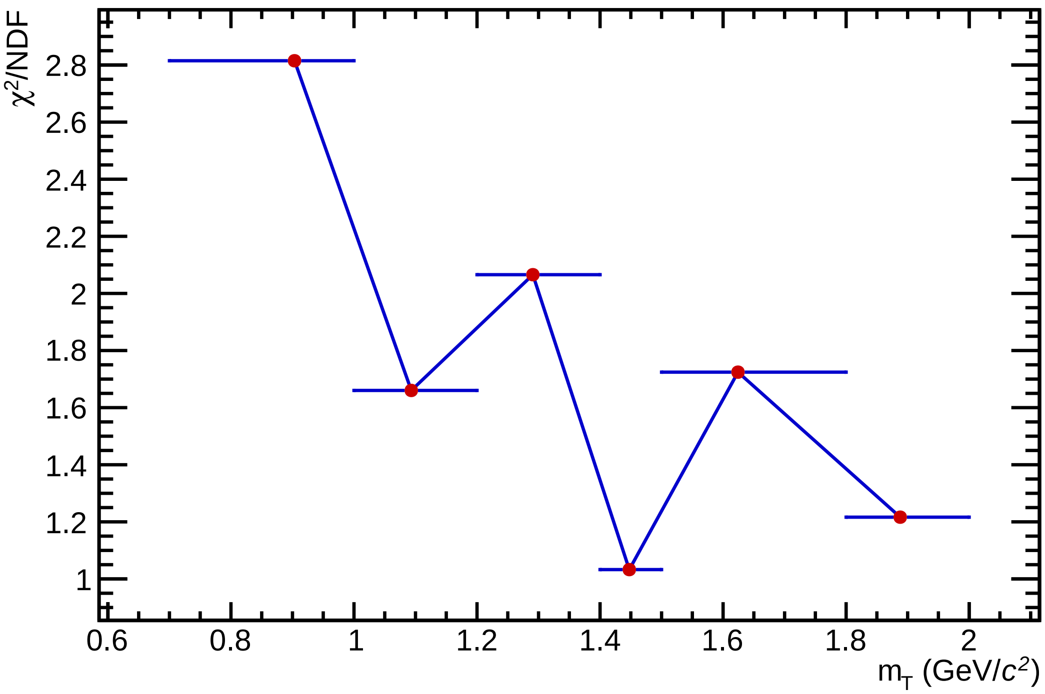

Figure 5.4: χ^2/NDF calculated for each m_T bin, calculated for $k^* \in [0, 400]$ MeV/c.

Variable	Default	Variation
Upper bound of k^* fit range (MeV/c)	400	350, 450
Effective resonance fractions	0.64 for proton, 0.48 for kaon	$\pm$ 10%
Effective resonance masses (MeV/c^2)	1362 for proton, 1050 for kaon	$\pm$ 10%
Effective resonance lifetimes (fm/c)	1.65 for proton, 3.66 for kaon	$\pm$ 10%
$\lambda_{\mathrm{flat}} = 1 - \lambda_{\mathrm{gen}}$	≈ 0.22	$\pm$ 10%

Table 5.2: Summary of systematic variations used for the RSM fits.

extracted from the default fit and a given systematic variation is taken as the systematic uncertainty for that variation. Adding together all systematic differences in quadrature produces an estimate for σ^2_{syst}, the square of the systematic uncertainty of r_{core}. To mitigate the contribution of variations which are not statistically significant a Barlow test is applied [46]. For the Barlow test, the Δr_{core} is compared to the difference in uncertainty between default and variation $\sigma_\Delta = (|\sigma^2_{var} - \sigma^2_{default}|)^{1/2}$. Every systematic variation for which $\Delta r_{\mathrm{core}}/\sigma_\Delta < 1$ is rejected from the overall systematic uncertainty of r_{core}. The systematic variations which pass the Barlow test and contribute to the uncertainties are summarised for each m_T bin in Fig. 5.5.

The extracted core source sizes from the fitting procedure are shown in Fig. 5.6. As is expected from the common source hypothesis, the source size decreases with increasing m_T. The results are compared with the scaling for proton-proton pairs, obtained in [4], shown in the figure as the blue points. The green band is a parametrisation within 3σ for the scaling of the source size with m_T, the values are taken from [47]. The results obtained here are consistent with the scaling of the proton-proton source size as the proton-proton band lies within the systematic uncertainties of the K^+-p scaling. Indeed, while the slope of the K^+-p scaling obtained here appears similar to that of the common scaling, the results lie consistently under the p-p values, especially for the first three m_T bins. This indicates a possible systematic error in the fitting procedure, which has not been accounted for in the current systematic uncertainties of r_{core}, resulting in a decrease of the core source size.

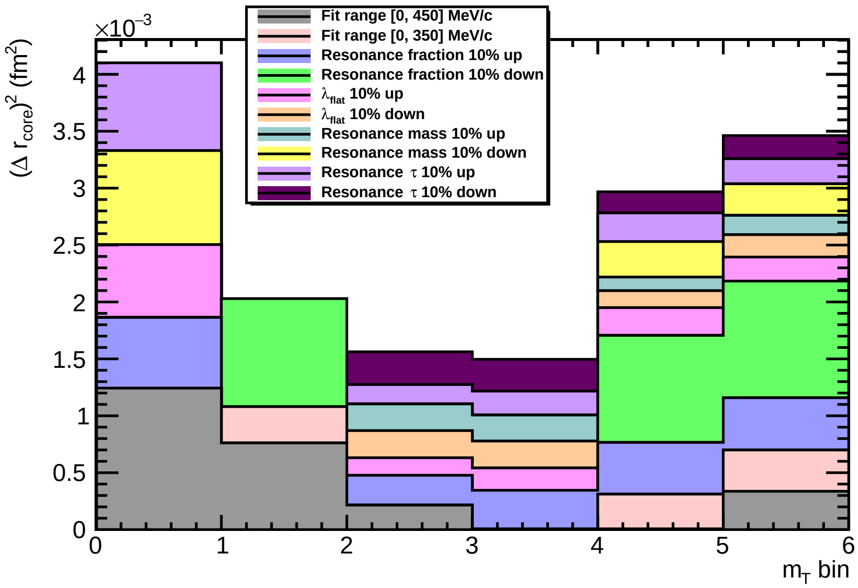

Figure 5.5: Systematic uncertainties for r_{core} obtained from RSM fits. The systematic variations tested are summarised in Tab. 5.2, this figure shows those that pass the Barlow test and contribute to the overall systematic uncertainties.

5.3 Results from CECA

The relative abundances for the resonances feeding into the source function computed with CECA are taken from Thermal-FIST [20]. Their p_{T} distributions are determined by a blast wave parametrisation [22]. For the fitting procedure of the CECA model to the experimental correlation function, these are fixed. The only parameters which are to be varied are r_d, h and τ, the variables responsible for determining the emission surface in CECA. In the case of the CECA model, the building of the source function is done through the generation of particles, using r_d, h and τ as parameters for their propagation. This is done until there are a sufficient number of particles in each m_{T} bin in order to minimise statistical uncertainties in the source functions. Varying any of the emission parameters means that the source needs to be built anew, so the traditional fitting procedure would take too much time to be a feasible method of determining the source.

For this reason, the optimization of the parameters is done using a grid scan method. Here, the parameters are varied as discrete values across a set range, and the source function is built with sufficient statistics for each combination (r_d, h, τ) of the parameters. The generated source functions are subsequently used to calculate the K$^+$-p correlations functions, which are fitted to the experimental data using Eq. (5.1) with $C_{\mathrm{genuine}}(k^*)$. To estimate the best choice of parameters from the given set, the χ^2 is calculated for each fit and the results for all m_{T} bins are added together. The combination of parameters with the lowest cumulative χ^2 is taken as the starting point for another grid scan, where the new parameters are varied across new smaller ranges centred at the starting points.

The emission variables are correlated, as variations in one parameter can be compensated by varying another. For example, a small increase in the initial displacement r_d can be compensated by a small decrease in the hadronisation surface parameter h, as this will produce a similarly sized overall source distribution. For this reason, in an attempt to find a solution in the parameter space which fits well with the experimental data, only r_d and τ are varied while h remains constant. The starting parameters $r'_d = 0.176$ fm, $\tau' = 3.76$ fm$/c$, and $h' = 2.68$ fm are those determined by fitting CECA to the proton-proton correlation function [5].

Two iterations of the grid scan are performed, the cumulative χ^2 results for the CECA fits are shown in the first 5 m_{T} bins in Fig. 5.7 and 5.8. The reason for only including the first 5 m_{T} ranges is

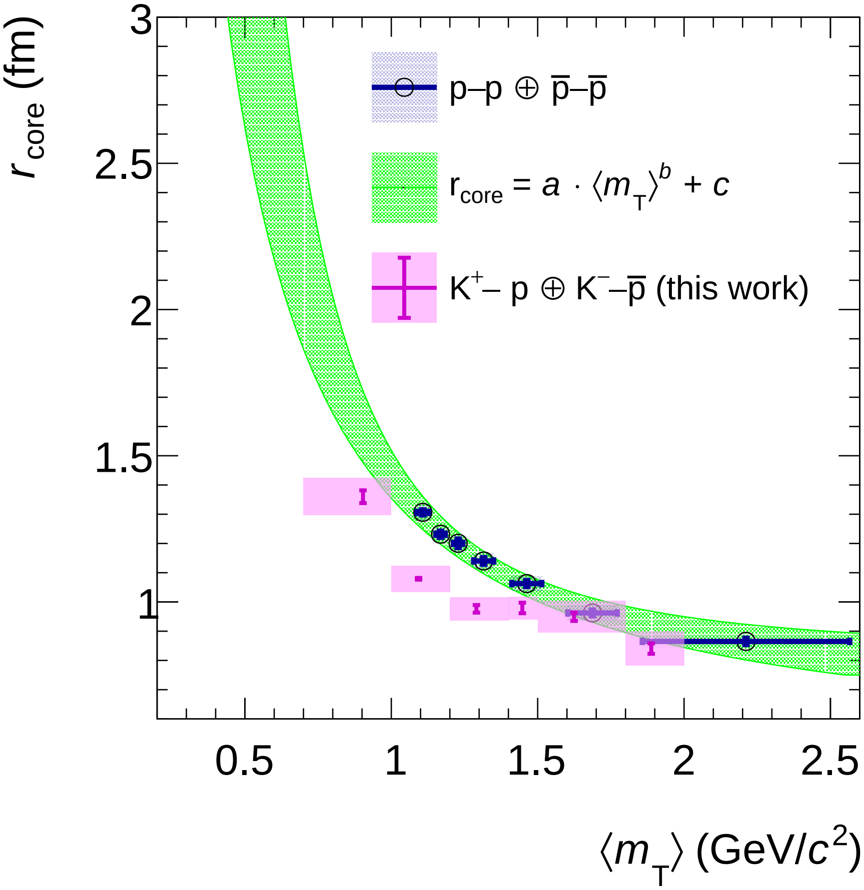

Figure 5.6: Extracted r_{core} values from fitting the resonance source model to data within different m_{T} bins, shown in pink, with statistical (lines) and systematic (shaded boxes) uncertainties. This is compared to the scaling of r_{core} for proton-proton correlations (blue points) together with the parametrisation of the scaling (green band). While the results exhibit a similar slope to that of the common scaling, the points lie under those obtained for p-p.

technical and unavoidable due to limitations of the RAM management of CATS. This, however, should not bias the optimization procedure discussed here. Both r_d and τ tend to lower values than those obtained in Ref. [5]. The χ^2 for varying τ across the range $[0.0, 5.0]$ fm/c forms a clear valley centered around $\tau = 2.6$ fm/c, suggesting that the optimal value for τ for this system is around this value. However, the χ^2 value does not change appreciably as r_d is varied over the range $[0.01, 0.21]$ fm, implying that the source function does not change much across this range.

The minimum of the cumulative χ^2 is found at the parameter set $r_d = 0.06$ fm, $h = 2.68$ fm and $\tau = 2.6$ fm/c. The source functions for CECA and RSM in the first m_{T} bin are shown in Fig. 5.9. The CECA source includes a more pronounced long range tail than the source function from the RSM. This corresponds to the resonances included in the CECA model with larger lifetimes than that of the effective resonance utilised in the resonance source model.

The result for the fit with the CECA correlation function in the first m_{T} bin is depicted in Fig. 5.10. The shape of the correlation function for CECA is in an approximate agreement with that for RSM, however the fit function tends to the edge of the uncertainties of the experimental data points. In contrast to that, the RSM function generally lies closer to the centres of the points. The CECA corre-

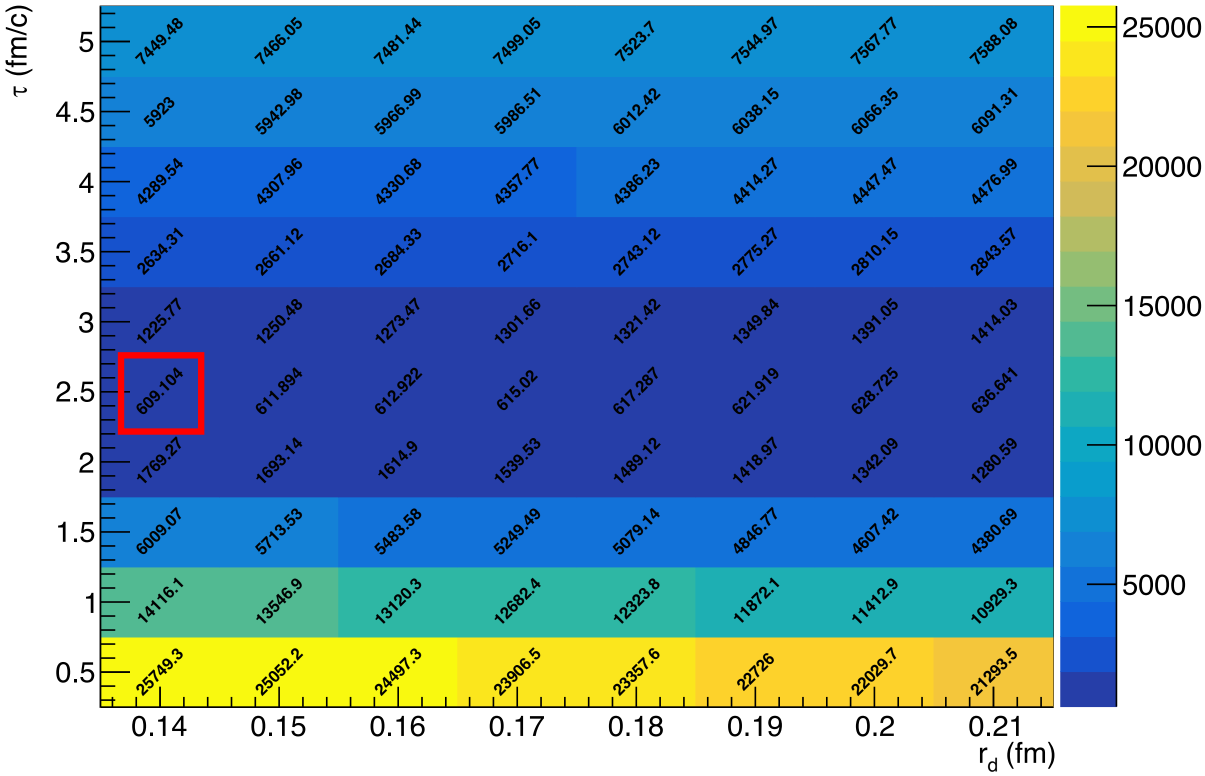

Figure 5.7: Cumulative χ^2 for the fits in the first 5 m_{T} bins, for the first iteration of the grid scan. The minimum, indicating the best fit, is highlighted in red.

lation functions for all other m_{T} bins are provided in App. B.2 and show a similar behaviour as described here.

At the present, the best reduced χ^2 from CECA ($\chi^2_{\mathrm{CECA}}/\mathrm{NDF} = 608/195 = 3.2$) is larger than the corresponding value for RSM ($\chi^2_{\mathrm{RSM}}/\mathrm{NDF} = 405/228 = 1.8$). However, given the complexities of the model, there is still a lot of room for improvement in determining the CECA source and correlation functions. The rudimentary grid scan approach is not enough to easily determine the best parameters for the source, especially if h is to be varied along with r_d and τ. Given the complexities of the parameter space, a machine learning approach might be the most suitable way to determine whether there is a definitive global minimum. In such a way, an actual fitting procedure for the parameters could be performed instead of a coarse grid scan.

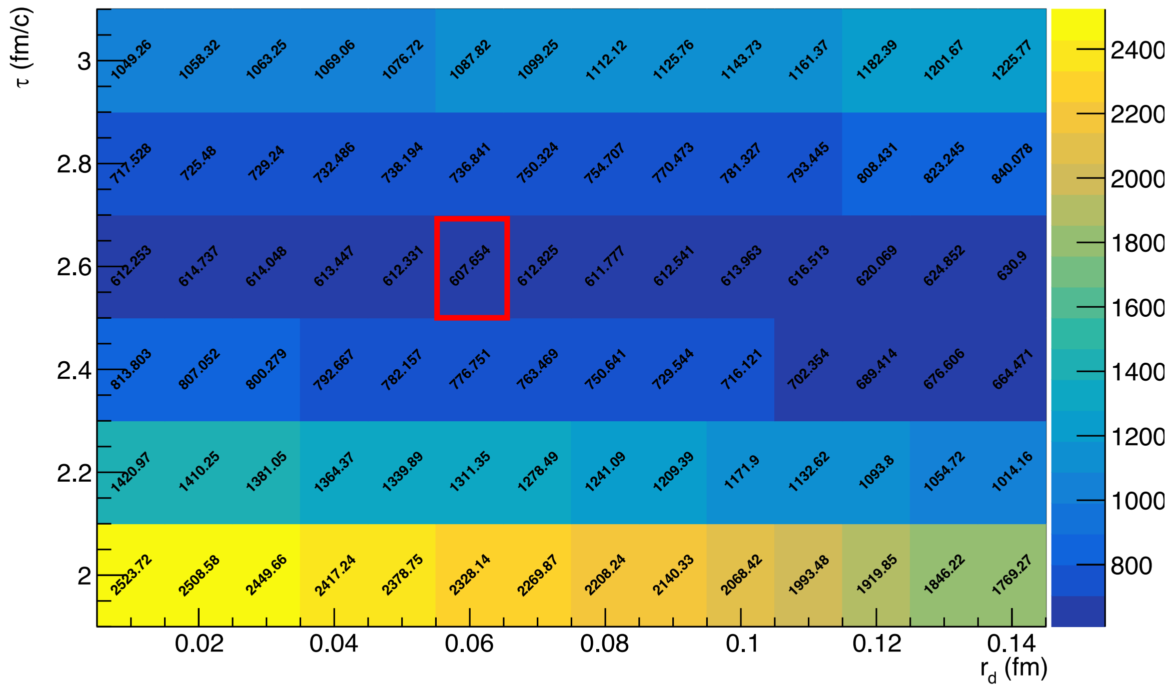

Figure 5.8: Cumulative χ^2 for the fits in the first 5 m_{T} bins, for the second iteration of the grid scan. The scan is performed across a range based the parameters of the minimum from the previous scan. The minimum at $r_d = 0.06$ fm, $h = 2.68$ fm and $\tau = 2.6$ fm/c is highlighted in red and is the final minimum found in the grid scan procedure.

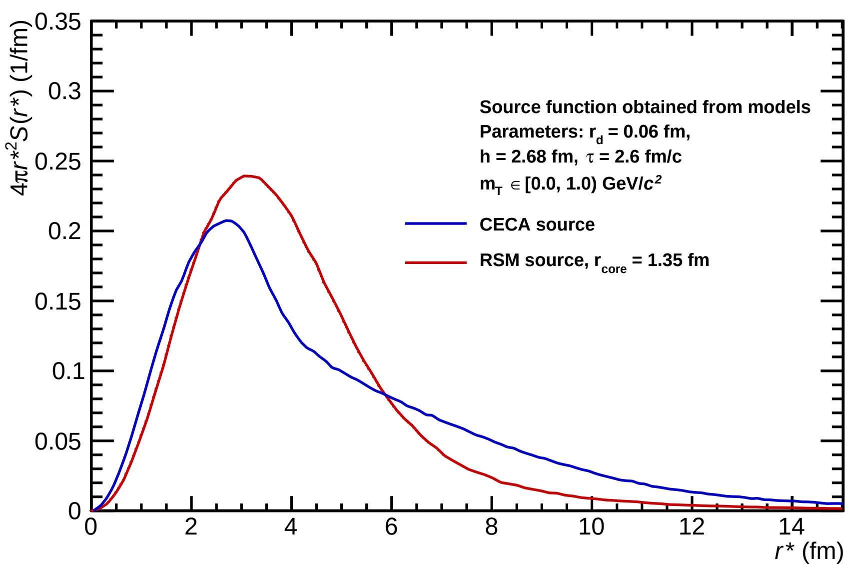

Figure 5.9: Comparison of the source function for both models in the first m_{T} bin. The RSM source is obtained through fitting to extract the core source size, whereas the CECA source is that corresponding to the ideal parameter set from the grid scan.

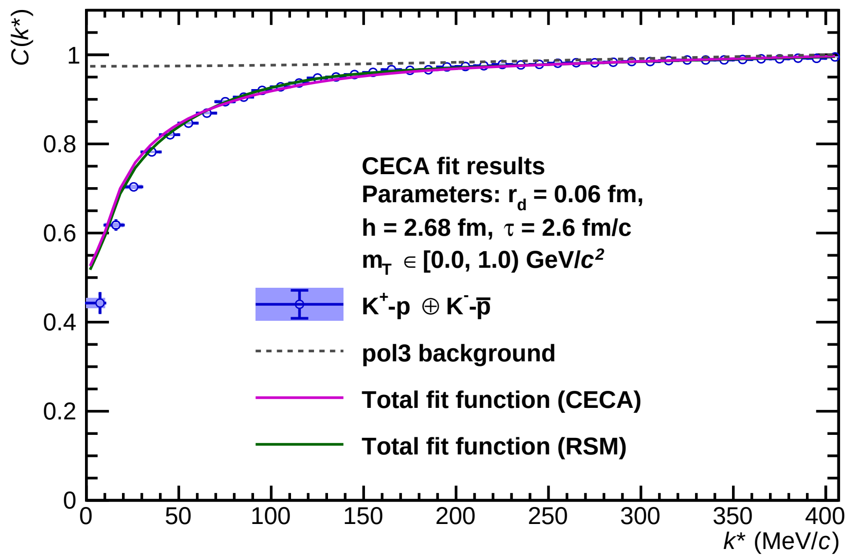

Figure 5.10: Fit results for the CECA correlation function, corresponding to the source shown in Fig. 5.9. As the polynomial background is fitted as a pre-fit, this leaves only the normalisation as a free parameter for fitting the CECA correlation function (pink line).

Chapter 6

Summary

In this thesis, the K^+−p correlation function has been measured for various m_T bins using high-multiplicity pp collisions at $\sqrt{s} = 13$ TeV recorded by ALICE at the LHC. The fractions and purities of the used proton and kaons have been investigated with the help of MC studies using Pythia 8.2 and GEANT3 [41, 42]. The extracted correlation functions are below unity for small relative momenta k^*, showing the repulsive interaction between kaons and protons. For larger relative momenta, the correlation function is not flat showing an additional non-femtoscopic background. The m_T differential correlation functions have been fitted using the χEFT [25, 26] interaction model and two different source models using CATS [17]. The fits include the effects of the residual background as well as feed-down from weakly decaying resonances. The latter is taken into account via the λ-parameters which have been investigated in an m_T differential way. Only a weak dependence of the λ-parameter on m_T for the K^+−p pairs has been found. Concerning the source study, firstly, the resonance source model (RSM) was employed which has been used in other source studies by ALICE for p−p and p−Λ correlations [4]. The fits with the RSM are in good agreement with the experimental data, yielding an overall $\chi^2_{\mathrm{RSM}}/\mathrm{NDF} = 405/228 = 1.8$. The extracted core source size for K^+−p exhibits the same common m_T as the aforementioned p−p and p−Λ systems and is consistent with those results within the uncertainties. However, especially the first three m_T seem to systematically lie below the common scaling which needs further investigation in the future. Secondly, the CECA source model has been investigated by comparing the correlation functions resulting from a coarse grid scan of r_d and τ for fixed h around the CECA parameters [5] obtained by fitting the p−p and p−Λ correlations. The optimal parameters found correspond to $r_d = 0.06$ fm, $h = 2.68$ fm and $\tau = 2.6$ fm/c and indicate a possible tension of a common CECA parameter set for baryon−baryon and meson−baryon correlations. The CECA prediction yields $\chi^2_{\mathrm{CECA}}/\mathrm{NDF} = 608/195 = 3.2$, and hence is less compatible with the data if compared to the RSM results. However, the optimization procedure needs to be improved by e.g. employing machine learning methods, before conclusive statements can be made. Finally, the systematic uncertainties pertaining to the fit itself (i.e. the variation of the λ−parameter, fit range, and so on) are missing in the CECA study, which biases the reduced χ^2_{CECA} to slightly higher values.

Appendix A

Data Analysis

A.1 Comparison pairs to anti-pairs

Figure A.1 shows the comparison between the correlation functions of K^+p and $K^-\bar{p}$. Both correlation functions are in agreement with each other within their statistical uncertainties for all presented m_T bins.

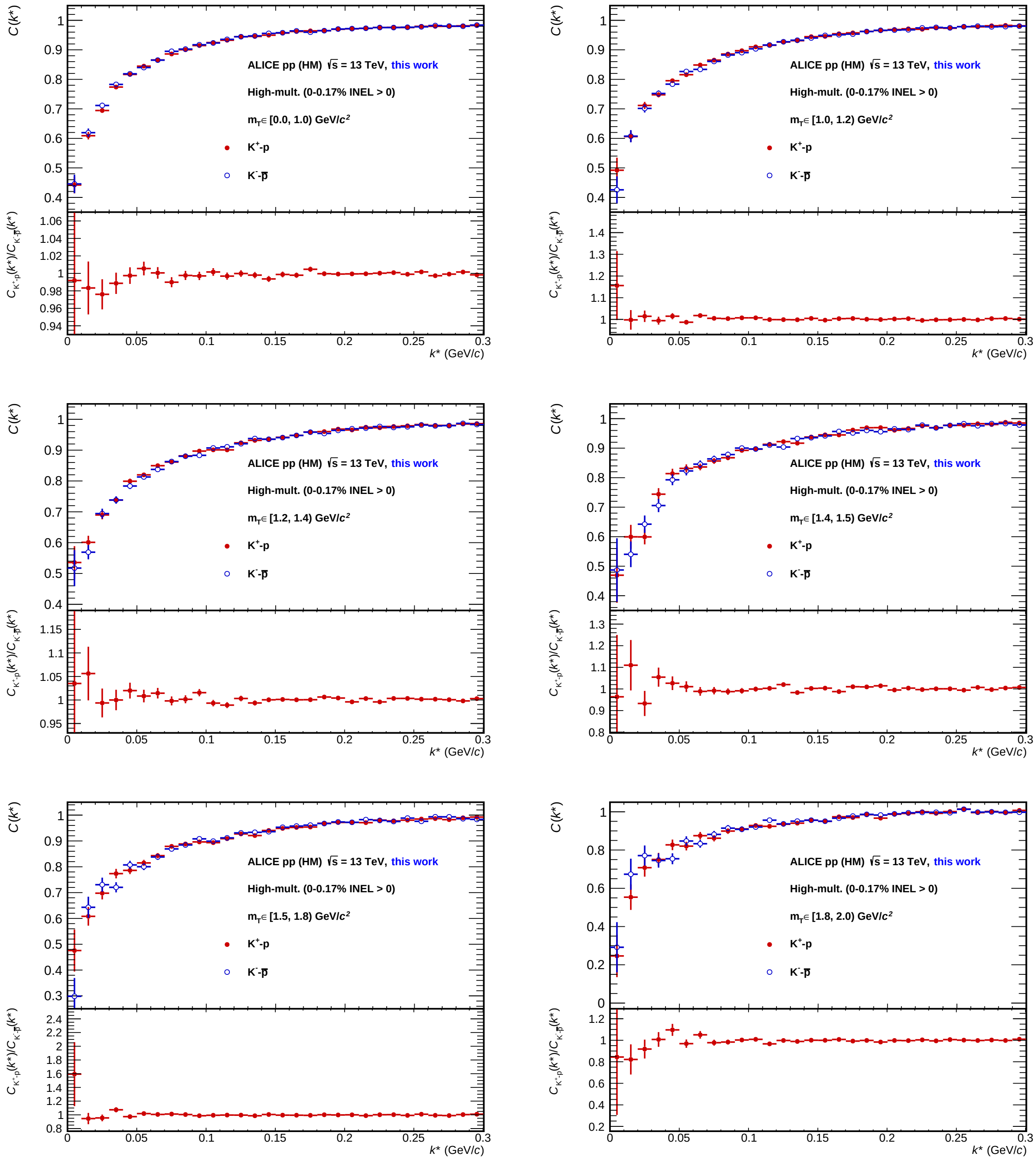

Figure A.1: Comparison between the correlation functions of K^+p and $K^-\bar{p}$.

A.2 Effects of multiplicity reweighting

Figure A.2 shows the comparison between the correlation functions when multiplicity reweighting described in Sec. 4.3.5 is and is not used. For all m_T bins differences can be observed for large relative momenta. However, in the low k^* region the two correlation functions are equal to each other .

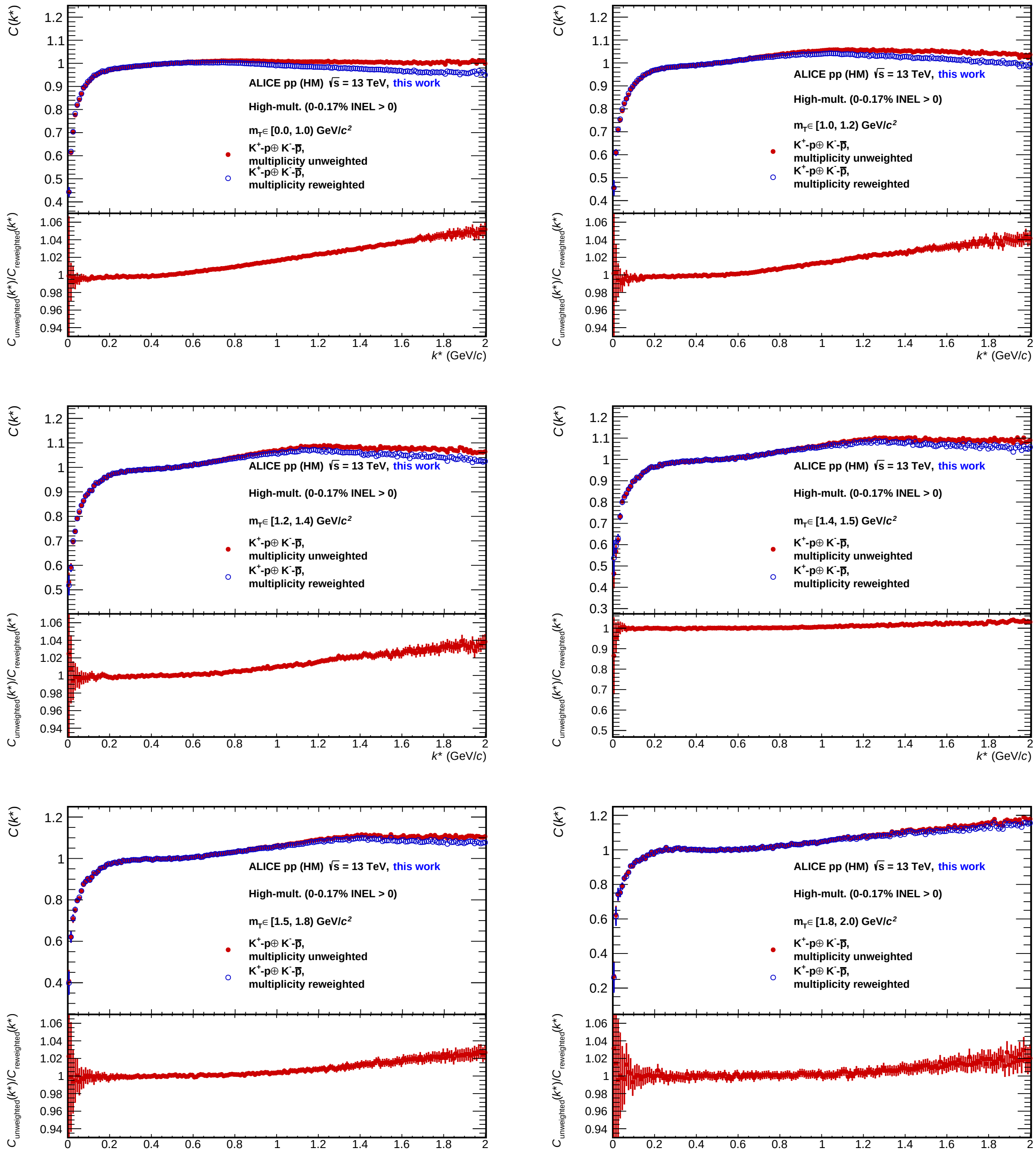

Figure A.2: Comparison between the correlation functions using and not using multiplicity reweighting.

Appendix B

Results

B.1 Pre-fits of non-femtoscopic background

Figure B.1 shows the pre-fit of the correlation function using the third-order polynomial Eq. (4.3) for all m_{T} bins. The pre-fits are perfomed in the range $k^* \in [275, 600]$ MeV/c and extrapolated down to zero relative momentum.

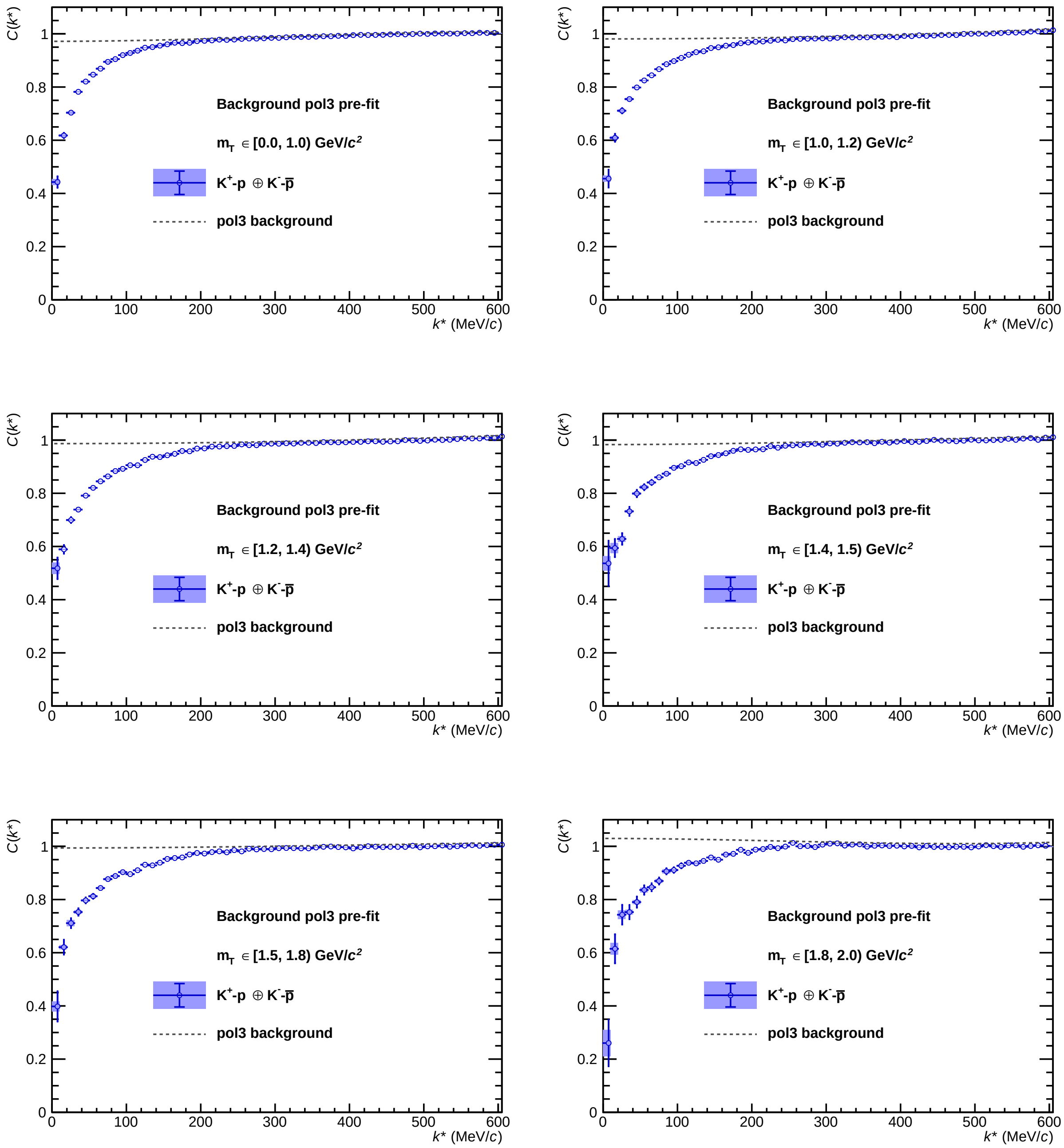

Figure B.1: Pre-fit of the non-femtoscopic background for all m_T bins. Statistical uncertainties of the data are shown with lines, systematic uncertainties are represented by boxes.

B.2 CECA correlation functions

Figure B.2 shows the CECA correlation functions for the second to fith m_T bin.

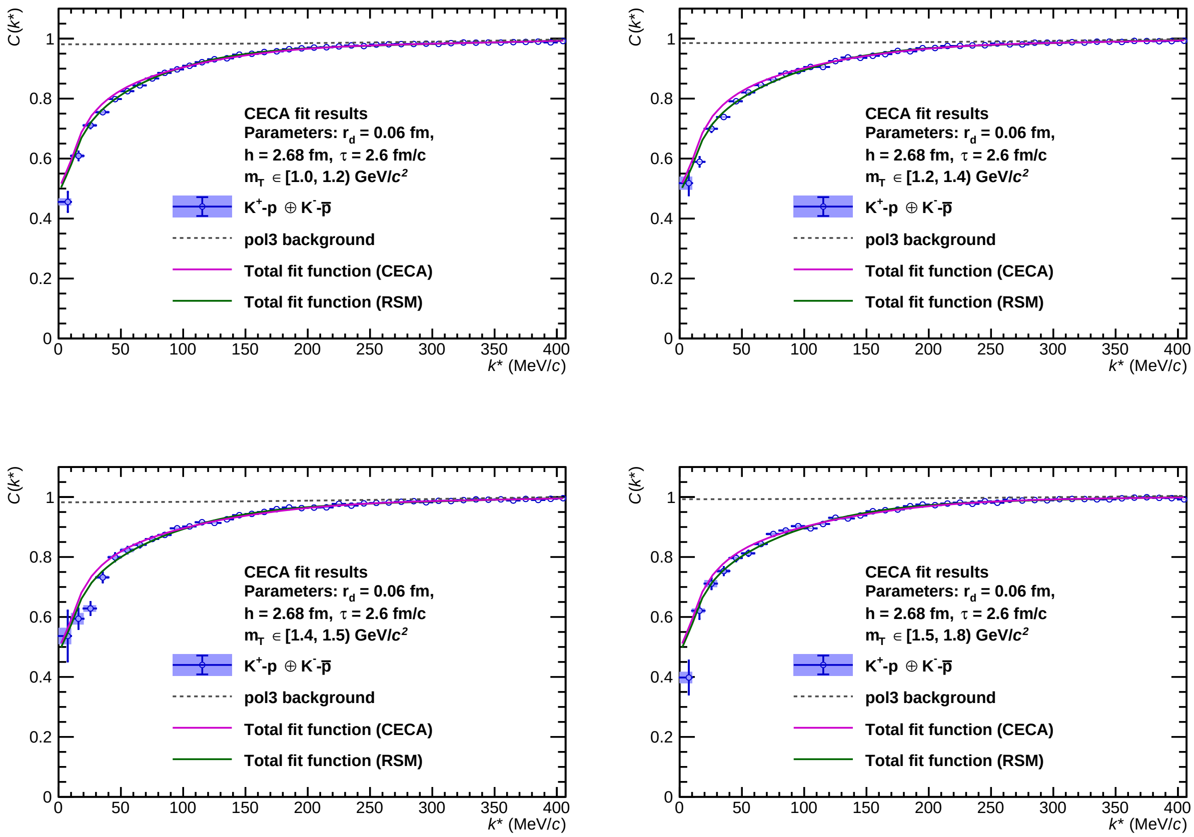

Figure B.2: Comparison of the correlation functions obtained with CECA to the RSM corrletion function and the experimental data. Statistical uncertainties of the data are shown with lines, systematic uncertainties are represented by boxes.

Bibliography

[1] **ALICE** Collaboration, S. Acharya *et al.*, "First study of the two-body scattering involving charm hadrons," *Phys. Rev. D* **106** no. 5, (2022) 052010, `arXiv:2201.05352 [nucl-ex]`.

[2] **ALICE** Collaboration, "First measurement of the Λ-Ξ interaction in proton-proton collisions at the LHC," `arXiv:2204.10258 [nucl-ex]`.

[3] **ALICE** Collaboration, A. Collaboration *et al.*, "Unveiling the strong interaction among hadrons at the LHC," *Nature* **588** (2020) 232–238, `arXiv:2005.11495 [nucl-ex]`. [Erratum: Nature 590, E13 (2021)].

[4] **ALICE** Collaboration, S. Acharya *et al.*, "Search for a common baryon source in high-multiplicity pp collisions at the LHC," *Phys. Lett. B* **811** (2020) 135849, `arXiv:2004.08018 [nucl-ex]`.

[5] D. Mihaylov and J. González González, "Novel model for particle emission in small collision systems," *Eur. Phys. J. C* **83** no. 7, (2023) 590, `arXiv:2305.08441 [hep-ph]`.

[6] J. Lattimer, "Neutron stars and the nuclear matter equation of state," *Annual Review of Nuclear and Particle Science* **71** no. 1, (2021) 433–464, `https://doi.org/10.1146/annurev-nucl-102419-124827`. `https://doi.org/10.1146/annurev-nucl-102419-124827`.

[7] Y. Kamiya, T. Hyodo, and A. Ohnishi, "Femtoscopic study on DD^* and $D\bar{D}^*$ interactions for T_{cc} and X(3872)," *Eur. Phys. J. A* **58** no. 7, (2022) 131, `arXiv:2203.13814 [hep-ph]`.

[8] **ALICE** Collaboration, S. Acharya *et al.*, "Constraining the $\overline{\mathrm{K}}$N coupled channel dynamics using femtoscopic correlations at the LHC," *Eur. Phys. J. C* **83** no. 4, (2023) 340, `arXiv:2205.15176 [nucl-ex]`.

[9] **ALICE** Collaboration, S. Acharya *et al.*, "Exploring the NΛ–NΣ coupled system with high precision correlation techniques at the LHC," *Phys. Lett. B* **833** (2022) 137272, `arXiv:2104.04427 [nucl-ex]`.

[10] L. Fabbietti, V. Mantovani Sarti, and O. Vazquez Doce, "Study of the Strong Interaction Among Hadrons with Correlations at the LHC," *Ann. Rev. Nucl. Part. Sci.* **71** (2021) 377–402, `arXiv:2012.09806 [nucl-ex]`.

[11] W. Busza, K. Rajagopal, and W. van der Schee, "Heavy Ion Collisions: The Big Picture, and the Big Questions," *Ann. Rev. Nucl. Part. Sci.* **68** (2018) 339–376, `arXiv:1802.04801 [hep-ph]`.

[12] M. A. Lisa, S. Pratt, R. Soltz, and U. Wiedemann, "Femtoscopy in relativistic heavy ion collisions," *Ann. Rev. Nucl. Part. Sci.* **55** (2005) 357–402, `arXiv:nucl-ex/0505014`.

[13] A. Kisiel, M. Gałażyn, and P. Bożek, "Pion, kaon, and proton femtoscopy in Pb–Pb collisions at $\sqrt{s_{\mathrm{NN}}}$=2.76 TeV modeled in (3+1)D hydrodynamics," *Phys. Rev. C* **90** no. 6, (2014) 064914, `arXiv:1409.4571 [nucl-th]`.

[14] G. Baym, "The Physics of Hanbury Brown-Twiss intensity interferometry: From stars to nuclear collisions," *Acta Phys. Polon. B* **29** (1998) 1839–1884, `arXiv:nucl-th/9804026`.

[15] **ALICE** Collaboration, S. Acharya *et al.*, "Pion-kaon femtoscopy and the lifetime of the hadronic phase in Pb−Pb collisions at $\sqrt{s_{\mathrm{NN}}} = 2.76$ TeV," *Phys. Lett. B* **813** (2021) 136030, `arXiv:2007.08315 [nucl-ex]`.

[16] **ALICE** Collaboration, S. Acharya *et al.*, "Kaon–proton strong interaction at low relative momentum via femtoscopy in Pb–Pb collisions at the LHC," *Phys. Lett. B* **822** (2021) 136708, arXiv:2105.05683 [nucl-ex].

[17] D. L. Mihaylov, V. Mantovani Sarti, O. W. Arnold, L. Fabbietti, B. Hohlweger, and A. M. Mathis, "A femtoscopic Correlation Analysis Tool using the Schrödinger equation (CATS)," *Eur. Phys. J. C* **78** no. 5, (2018) 394, arXiv:1802.08481 [hep-ph].

[18] **ALICE** Collaboration, J. Adam *et al.*, "One-dimensional pion, kaon, and proton femtoscopy in Pb-Pb collisions at $\sqrt{s_{\mathrm{NN}}}$ =2.76 TeV," *Phys. Rev. C* **92** no. 5, (2015) 054908, arXiv:1506.07884 [nucl-ex].

[19] F. Becattini, "An Introduction to the Statistical Hadronization Model," in *International School on Quark-Gluon Plasma and Heavy Ion Collisions: past, present, future.* 1, 2009. arXiv:0901.3643 [hep-ph].

[20] V. Vovchenko and H. Stoecker, "Thermal-FIST: A package for heavy-ion collisions and hadronic equation of state," *Comput. Phys. Commun.* **244** (2019) 295–310, arXiv:1901.05249 [nucl-th].

[21] T. Pierog, I. Karpenko, J. M. Katzy, E. Yatsenko, and K. Werner, "EPOS LHC: Test of collective hadronization with data measured at the CERN Large Hadron Collider," *Phys. Rev. C* **92** no. 3, (2015) 034906, arXiv:1306.0121 [hep-ph].

[22] S. Grigoryan, "A three component model for hadron p_{T}-spectra in pp and Pb–Pb collisions at the LHC," *Eur. Phys. J. A* **57** no. 12, (2021) 328, arXiv:2109.07888 [hep-ph].

[23] S. Weinberg, "Nuclear forces from chiral lagrangians," *Physics Letters B* **251** no. 2, (1990) 288–292. https://www.sciencedirect.com/science/article/pii/037026939090938 3.

[24] H. Sazdjian, "Introduction to chiral symmetry in QCD," *EPJ Web Conf.* **137** (2017) 02001, arXiv:1612.04078 [hep-ph].

[25] D. Hadjimichef, J. Haidenbauer, and G. Krein, "Short range repulsion and isospin dependence in the KN system," *Phys. Rev.* **C66** (2002) 055214, arXiv:nucl-th/0209026 [nucl-th].

[26] K. Aoki and D. Jido, "KN scattering amplitude revisited in a chiral unitary approach and a possible broad resonance in S = +1 channel," *PTEP* **2019** no. 1, (2019) 013D01, arXiv:1806.00925 [nucl-th].

[27] A. Hoecker, "Physics at the LHC Run-2 and Beyond," in *2016 European School of High-Energy Physics.* 11, 2016. arXiv:1611.07864 [hep-ex].

[28] J. T. Boyd, "LHC Run-2 and future prospects," *CERN Yellow Rep. School Proc.* **5** (2022) 247, arXiv:2001.04370 [hep-ex].

[29] A. Tauro, "ALICE Schematics." General Photo, 2017.

[30] **ALICE** Collaboration, B. B. Abelev *et al.*, "Performance of the ALICE Experiment at the CERN LHC," *Int. J. Mod. Phys. A* **29** (2014) 1430044, arXiv:1402.4476 [nucl-ex].

[31] **ALICE** Collaboration, E. Abbas *et al.*, "Performance of the ALICE VZERO system," *JINST* **8** (2013) P10016, arXiv:1306.3130 [nucl-ex].

[32] **ALICE** Collaboration, K. Aamodt *et al.*, "The ALICE experiment at the CERN LHC," *JINST* **3** (2008) S08002.

[33] **ALICE** Collaboration, V. Manzari, "The ALICE Inner Tracking System: Commissioning and running experience," *PoS* **VERTEX2009** (2009) 005.

[34] **ALICE** Collaboration, C. Zampolli, "Particle Identification with the ALICE detector at the LHC," in *PLHC2012: Physics at the LHC 2012.* 9, 2012. arXiv:1209.5637 [hep-ex].

[35] J. Alme and Y. A. et. al., "The ALICE TPC, a large 3-dimensional tracking device with fast readout for ultra-high multiplicity events," *Nuclear Instruments and Methods in Physics Research Section A: Accelerators, Spectrometers, Detectors and Associated Equipment* **622** no. 1, (Oct, 2010) 316–367. `https://doi.org/10.1016%2Fj.nima.2010.04.042`.

[36] **ALICE TPC** Collaboration, J. Adolfsson *et al.*, "The upgrade of the ALICE TPC with GEMs and continuous readout," *JINST* **16** no. 03, (2021) P03022, `arXiv:2012.09518 [physics.ins-det]`.

[37] A. P. Kalweit, "ALICE TPC dE/dx performance in Run2 13 TeV (0.2T)." 2015.

[38] **ALICE** Collaboration, G. Dellacasa *et al.*, "ALICE technical design report of the time-of-flight system (TOF),".

[39] **ALICE** Collaboration, N. Jacazio, "PID performance of the ALICE-TOF detector at Run 2," *PoS* **LHCP2018** (2018) 232, `arXiv:1809.00574 [physics.ins-det]`.

[40] R. T. J. Bustamante, "TOF beta vs momentum performance in pp at 13 TeV (LHC15f)." TOF beta vs Momentum performance plot in pp at 13 TeV, 2016.

[41] T. Sjostrand, S. Mrenna, and P. Z. Skands, "PYTHIA 6.4 Physics and Manual," *JHEP* **05** (2006) 026, `arXiv:hep-ph/0603175`.

[42] **ALICE** Collaboration, S. Acharya *et al.*, "Study of the Λ-Λ interaction with femtoscopy correlations in pp and p-Pb collisions at the LHC," *Phys. Lett. B* **797** (2019) 134822, `arXiv:1905.07209 [nucl-ex]`.

[43] **ALICE** Collaboration, J. Adam *et al.*, "Enhanced production of multi-strange hadrons in high-multiplicity proton-proton collisions," *Nature Phys.* **13** (2017) 535–539, `arXiv:1606.07424 [nucl-ex]`.

[44] **ALICE** Collaboration, B. Abelev *et al.*, "Transverse sphericity of primary charged particles in minimum bias proton-proton collisions at $\sqrt{s} = 0.9$, 2.76 and 7 TeV," *Eur. Phys. J. C* **72** (2012) 2124, `arXiv:1205.3963 [hep-ex]`.

[45] **ALICE** Collaboration, S. Acharya *et al.*, "p-p, p-Λ and Λ-Λ correlations studied via femtoscopy in pp reactions at $\sqrt{s} = 7$ TeV," *Phys. Rev. C* **99** no. 2, (2019) 024001, `arXiv:1805.12455 [nucl-ex]`.

[46] R. Barlow, "Systematic errors: Facts and fictions," in *Conference on Advanced Statistical Techniques in Particle Physics*, pp. 134–144. 7, 2002. `arXiv:hep-ex/0207026`.

[47] A. Mathis, "First Measurement of the Proton-Sigma0 Interaction via the Femtoscopy Method," *Phd Thesis* (2020) .